














Publication Year	2022
Acceptance in OA @INAF	2023-07-24T14:56:11Z
Title	The complex stellar system M 22: confirming abundance variations with high precision differential measurements
Authors	McKenzie, M; Yong, D; MARINO, Anna; Monty, S; Wang, E; et al.
DOI	10.1093/mnras/stac2254
Handle	http://hdl.handle.net/20.500.12386/34331
Journal	MONTHLY NOTICES OF THE ROYAL ASTRONOMICAL SOCIETY
Number	516

The complex stellar system M 22: confirming abundance variations with high precision differential measurements

M. McKenzie ^{1,2}★, D. Yong ^{1,2}, A. F. Marino ^{3,4}, S. Monty ^{1,2}, E. Wang ^{1,2}, A. I. Karakas ^{2,5},
A. P. Milone ^{3,6}, M. V. Legnardi ⁶, I. U. Roederer ^{7,8}, S. Martell ^{2,9} and D. Horta ¹⁰

¹Research School of Astronomy & Astrophysics, Australian National University, Canberra, ACT 2611, Australia

²ARC Centre of Excellence for Astrophysics in Three Dimensions (ASTRO-3D), Australia

³Istituto Nazionale di Astrofisica - Osservatorio Astronomico di Padova, Vicolo dell'Osservatorio 5, I-35122 Padua, Italy

⁴Istituto Nazionale di Astrofisica - Osservatorio Astrofisico di Arcetri, Largo Enrico Fermi, 5, I-50125 Firenze, Italy

⁵School of Physics & Astronomy, Monash University, Clayton, VIC 3800, Australia

⁶Dipartimento di Fisica e Astronomia 'Galileo Galilei,' Università di Padova, Vicolo dell'Osservatorio 3, I-35122 Padua, Italy

⁷Department of Astronomy, University of Michigan, 1085 S. University Ave., Ann Arbor, MI 48109, USA

⁸Joint Institute for Nuclear Astrophysics – Center for the Evolution of the Elements (JINA-CEE), USA

⁹School of Physics, University of New South Wales, Sydney, NSW 2052, Australia

¹⁰Astrophysics Research Institute, Liverpool John Moores University, 146 Brownlow Hill, Liverpool L3 5RF, UK

Accepted 2022 July 27. Received 2022 July 17; in original form 2022 May 31

ABSTRACT

M 22 (NGC 6656) is a chemically complex globular cluster-like system reported to harbour heavy element abundance variations. However, the extent of these variations and the origin of this cluster is still debated. In this work, we investigate the chemical in-homogeneity of M 22 using differential line-by-line analysis of high-quality ($R = 110\,000$, $S/N = 300$ per pixel at 514 nm) VLT/UVES spectra of six carefully chosen red giant branch stars. By achieving abundance uncertainties as low as ~ 0.01 dex (~ 2 per cent), this high precision data validates the results of previous studies and reveals variations in Fe, Na, Si, Ca, Sc, Ti, Cr, Mn, Co, Ni, Zn, Y, Zr, La, Ce, Nd, Sm, and Eu. Additionally, we can confirm that the cluster hosts two stellar populations with a spread of at least 0.24 dex in $[Fe/H]$ and an average s -process abundance spread of 0.65 dex. In addition to global variations across the cluster, we also find non-negligible variations within each of the two populations, with the more metal-poor population hosting larger spreads in elements heavier than Fe than the metal-rich. We address previous works that do not identify anomalous abundances and relate our findings to our current dynamical understanding of the cluster. Given our results, we suggest that M 22 is either a nuclear star cluster, the product of two merged clusters, or an original building block of the Milky Way.

Key words: techniques: spectroscopic – stars: abundances – stars: Population II – globular clusters: general – globular clusters: individual: NGC 6656.

1 INTRODUCTION

Deciphering the formation mechanisms of globular clusters (GCs) is a major challenge for both theorists and observers. Many early efforts to characterise these stellar systems assumed that they consisted of simple stellar populations with a single age, helium abundance, and overall metallicity. However, there are always exceptions to every rule. One such exception is the enigmatic cluster M 22, which happens to be one of the first clusters to be studied in detail (Shapley 1930b; Sawyer 1944; Arp & Melbourne 1959). Historically, M 22 has often been compared to ω Centauri (ω Cen; Shapley 1930a); a probable dwarf galaxy nucleus candidate (Bekki & Freeman 2003). However M 22 was considered to be a less extreme version of the cluster (Hesser, Hartwick & McClure 1976; Hesser, Hartwick & McClure 1977). Hesser & Harris 1979 builds upon Lloyd Evans 1978a and describes four different factors which contributed to this hypothesis.

(1) For stars lying on or near the red giant branch (RGB), David Dunlap Observatory photometry showed a wide range of both metal

and CN indices [for example, for M 22 see Norris & Freeman (1983), and for ω Cen see Freeman & Rodgers 1975, Norris & Bessell 1975 or Lloyd Evans 1977]. This is a manifestation of what we now understand to be the multiple stellar population phenomenon (for reviews on this topic, see Kraft 1994, Gratton, Carretta & Bragaglia 2012, Bastian & Lardo 2018 and Gratton et al. 2019).

(2) Both clusters were found to contain Barium stars (Mallia 1976a; Mallia 1976b) and probable CH stars (Harding 1962; Bond 1975; Hesser et al. 1977). At the time, no other clusters were known to contain these anomalous stars. Today, these represent s -process enhanced populations that have since emerged in several clusters (Norris & Da Costa 1995; Smith et al. 2000; Yong & Grundahl 2008; Carretta et al. 2011; Carretta et al. 2013; Yong et al. 2014a; Marino et al. 2015). s -process elements refer to elements heavier than iron synthesized via the slow neutron-capture process, which occurs in the He-shells of low-mass asymptotic giant branch (AGB) stars. (e.g. Clayton et al. 1961; Busso, Gallino & Wasserburg 1999; Karakas & Lattanzio 2014; Kobayashi, Karakas & Lugaro 2020).

(3) The colour magnitude diagram (CMD) of M 22 appeared to show similar characteristics to the ‘wide giant-branch’ phenomenon identified in ω Cen (Woolley 1966; Cannon & Stobie 1973; Bessell &

* E-mail: madeleine.mckenzie@anu.edu.au

Norris 1976). Later, Marino et al. (2009) and Piotto et al. (2012) also found a broadened sub-giant branch, indicative of stellar populations with different C + N + O abundances or different ages (Cassisi et al. 2008). While significant reddening was excluded as a possible cause in ω Centauri (Cannon 1980), M 22 is situated at the edge of the dense star clouds of Sagittarius near the Galactic plane (Shapley & Duncan 1922), and thus it is unsurprising that Richter, Hilker & Richtler (1999) found differential reddening in the direction of M 22. However despite this, Monaco et al. (2004) could not rule out the presence of a small metallicity spread.

(4) There appeared to be flattening of both clusters that was correctly interpreted as rotation of the cluster [early observations include Lindsay (1956) with supporting theoretical models from King (1961)]. Internal rotation within GCs has since been confirmed by several studies such as Bianchini et al. (2013, 2018), Lardo et al. (2015), Kamann et al. (2018), and Cordoni et al. (2020a). Recently, Cordoni et al. (2020b) combined multiband photometry from the *Hubble Space Telescope* (*HST*) and ground-based facilities with *Gaia* Data Release 2 and *HST* proper motions to analyse the kinematics of both ω Cen and M 22. Both clusters share many kinematic qualities; stellar populations with different metallicities share similar motions, ellipticity and have rotation patterns with similar phases and amplitudes.

This naturally leads to the suggestion that, like ω Cen, M 22 is the nucleus of a dwarf galaxy (e.g. Bekki & Freeman 2003). This small, but growing, class of clusters, known as ‘Type II’ clusters (Milone et al. 2017), exhibits dispersions in metallicity and/or *s*-process element abundances and includes, but is not limited to, ω Cen, Terzan 5, M54, and M2 (Norris & Da Costa 1995; Carretta et al. 2010a; Yong et al. 2014b; McKenzie & Bekki 2018). This is juxtaposed by ‘Type I’ GCs, which exhibit homogeneous heavy element abundances (Carretta et al. 2009). However, emerging research demonstrates that even some Type I GCs exhibit metallicity variation among their primordial population as inferred from photometry and spectroscopy (Yong et al. 2013; Marino et al. 2019; Legnardi et al. 2022).

Many studies suggest that M 22 is indeed a Type II cluster. However, the possibility that M 22 is a nucleated dwarf remains an unresolved issue (Mucciarelli et al. 2015; Pfeffer et al. 2021). An extensive compilation of literature on the topic of whether M 22 contains intrinsic metallicity variations is given in Table 1.

Higher precision abundance measurements may provide new insight into the existence of a metallicity spread in M 22. Studies that reach uncertainties as low as ~ 0.01 dex (~ 2 per cent; Yong et al. 2013) have had great success in validating abundance variations and disentangling formation sources of GCs. Therefore, the aim of this paper is to use similar high precision abundance measurements to confirm or disprove metallicity ([Fe/H]) and other abundance variations beyond reasonable doubt. To achieve this, we reduce the uncertainties in the element abundances by adopting a differential analysis.

In Section 2, we discuss our target selection and stellar parameter determination. We present our result from our differential abundance measurements in Section 3, our discussion in Section 4 and conclusion in Section 5.

2 OBSERVATIONS AND ANALYSIS

2.1 Target selection and observations

We select our program stars from Marino et al. (2011). The spectra analysed by Marino et al. (2011) were visually examined to identify stars with detectable MgH molecular lines to be used for future isotopic analysis. Such analysis requires high-resolution and signal-

to-noise ratio (S/N) spectra, thus six stars were re-observed with UVES (Dekker et al. 2000) on the ESO VLT UT2 telescope. Three of these belong to the *s*-process poor group as identified by Marino et al. (2011), and the remaining three are from the *s*-process rich population.

The observations were taken using image slicer #3 and the 0′.3 slit. Exposure times for each star ranged from 1.5 to 2.1 h. We used the 580 nm setting that provided wavelength coverage from ~ 4800 to ~ 6800 Å, with a small gap near 5800 Å due to the space between the two CCDs in the UVES camera. There were no detected neighbours within the entrance aperture (1.5×2.0 arcsec) of the image slicer which minimizes contamination. The spectra were reduced using the ESO pipeline, and radial velocities were estimated using IRAF. The spectra for each star has a resolution of $R = 110\,000$ and $S/N \geq 300$ per pixel near 514 nm. We present measurements of the heliocentric radial velocities in Table A1, which are in agreement with literature values.

Fig. 1 shows the RGB, Na-O anticorrelation and [La/Eu] as a function of [Fe/H] for the program stars. In the left-hand panel, we use the G, BP, and RP filters from *Gaia* EDR3 (Gaia Collaboration 2021) to illustrate that our sample consists of stars exclusively located near the tip of the RGB. The brightest and faintest stars have G band magnitudes of 10.83 and 10.26, respectively. The centre and right-hand panels both leverage the complete data set from Marino et al. (2011) with *s*-process rich targets shown in red pentagons (C, III-52, and III-3) and *s*-process poor targets in blue crosses (III-15, III-14, and IV-102). The range of light element abundances for the Na-O anticorrelation is highlighted in the centre, and the distinction between the two *s*-process groups is given on the left.

We present an example of our spectra in Fig. 2 over the *s*-process line La II and iron peak elements Cr I, Ti I, and Fe I. Visual inspection reveals that the *s*-process rich stars exhibit stronger absorption lines than the *s*-process poor stars (blue). The extremely high quality of the spectra, combined with the technique of differential analysis, enables us to achieve relative abundance measurements with uncertainties as low as 2 per cent (0.01 dex).

2.2 Line list and equivalent width measurements

Our line list is an amalgamation of three lists recently used in the literature. First, we use atomic data from Ji et al. (2020), which was obtained using the program LINEMAKE¹ (Placco et al. 2021). Next, lines were also taken from Battaglia et al. (2017, which in turn is assembled from Roederer et al. 2008 and Roederer et al. 2010 and others), as well as the RGB tip line list used in Yong et al. (2013). Because of our differential approach, errors in the atomic data will largely cancel (Meléndez et al. 2009; Nissen & Gustafsson 2018).

We developed and implemented a new code Routine for EValuating and Inspecting Equivalent Widths (REVIEW²) that fits individual absorption lines using the `scipy.optimize` function `curve_fit` and a feedforward neural network (FFNN; Goodfellow, Bengio & Courville 2016) trained on synthetic spectra. However, we do not solely rely on the FFNN as it was not trained on data that contain hyperfine and isotopic splitting. Thus we compare the output of the FFNN with a Gaussian function and select the model with the smallest residuals. We discuss this new code further in Appendix B.

To ensure our code is producing reliable results, we compare the equivalent widths (EWs) from REVIEW and DAOSPEC (Stetson &

¹<https://github.com/vmplacco/linemake>

²<https://github.com/madeleine-mckenzie/REVIEW>

Table 1. Publications on M 22 abundances and whether they report an iron or other light element abundance spread within the cluster. We do not guarantee that this is an exhaustive list, and we do not include works that approach this problem from a theoretical perspective. Any references to tables relate to the publication listed in that row.

Publication	Fe spread?	Other element spread?	Comments
Manduca & Bell (1978)	No	No	Ca abundance of RR Lyrae variables. Data from Butler et al. (1973).
Peterson (1980)	Yes, 0.56 dex difference	Not discussed	Four stars in the sample.
Cohen (1981)	No	0.8 dex difference in Na	Three stars in the sample.
Gratton (1982)	No	No	Three stars in the sample.
Pilachowski et al. (1982)	Yes, 0.5 dex difference	Yes	Six stars in the sample.
Norris & Freeman (1983)	Not discussed	Ca, CH and CN variations	Using photometry.
Frogel, Persson & Cohen (1983)	Not discussed	‘Tremendous range’ in CN	Using infrared photometry.
Wallerstein, Leep & Oke (1987)	Sample size too small (0.2 dex between stars)	Al and Ti	Two stars.
Gratton & Ortolani (1989)	Yes, see Table 5	Yes, see abundances in Table 5	Three stars.
Brown, Wallerstein & Oke (1990)	Yes, 0.3 dex with non uniform reddening, 0.4 dex with uniform reddening	Notable N spread	Six stars in the sample. Stellar parameters originating from Frogel et al. (1983), Cudworth (1986) & Norris & Freeman (1983)
Lehnert, Bell & Cohen (1991)	Yes, 0.31 dex, see Table 5	Yes, [Ca/H] correlated with [Na/H]	10 stars, using Ca triplet.
Laird, Wilhelm & Peterson (1991)	No	Not discussed	26 giant stars.
Brown & Wallerstein (1992)	Yes, 0.19 dex	Yes, see Table 5	Spectra used is a subset of Brown et al. (1990). Values from Table 5 CN strong and weak stars.
Anthony-Twarog, Twarog & Craig (1995)	No (‘a spread of less than 0.2 dex cannot be excluded’)	Confirm correlation between Ca and CN/CH as in Norris & Freeman (1983)	Using uvbyCa photometry.
Richter et al. (1999)	No	Large dispersion of CN strength	Using Stromgren photometry.
Monaco et al. (2004)	No, (maximum allowed spread of $\Delta[\text{Fe}/\text{H}] \simeq 0.1\text{--}0.2$ dex)	Not discussed	Wide field photometry. Emphasizes reddening in the cluster.
Marino et al. (2009)	Yes, average difference of 0.15 dex	Yes, see Table 6	17 stars in the sample.
Da Costa et al. (2009)	Yes, IQR of metal rich and poor populations is 0.24 dex	Yes, Ca	55 candidate red giants in the field. Based on Ca triplet.
Lee et al. (2009)	Yes	Yes, Ca	Ca hk index of the Ca-by photometry.
Marino et al. (2011)	Yes, ‘substantial star-to-star metallicity scatter ($-2.0 \lesssim [\text{Fe}/\text{H}] \lesssim -1.6$)’	Yes, $\Delta[\text{C}+\text{N} + \text{O}/\text{Fe}] \approx 0.13$ dex	35 red giant stars.
Roederer, Marino & Sneden (2011)	Yes	Yes, <i>s</i> and <i>r</i> process materials	Six RGB stars.
Alves-Brito et al. (2012)	Yes, $\Delta[\text{Fe}/\text{H}] = 0.43$ dex	Yes, large C and N abundance spreads, 0.6 dex variation in F	11 stars. Based on IR.
Joo & Lee (2013)	Yes, $\Delta[\text{Fe}/\text{H}] = 0.25$ dex	Yes, $\Delta Y = 0.09 \pm 0.04$	Population models. Best fitting model age difference of 0.3 ± 0.4 Gyr.
Marino, Milone & Lind (2013)	Yes, see Table 2	Yes, see Table 2	Seven stars on the HB, main purpose to measure Ba and Na abundances.
D’Orazi et al. (2013)	Not discussed	Yes, F variations	Near-infrared CRIRES spectroscopic observations of six cool giant stars.
Gratton et al. (2014)	Yes, see Table 5	Yes, see Table 5	94 candidate stars belonging to the HB.
Lim et al. (2015)	Yes, $\Delta[\text{Fe}/\text{H}] = 0.18$ dex	Yes, Ca. Also a CN bimodality	New narrow-band Ca photometry. As in Lee et al. (2009) but without contamination from CN bands.
Mucciarelli et al. (2015)	No	Yes, <i>s</i> -process variations	UVES and UVES-FLAMES of 17 giants.
Lee (2016)	Yes	Yes	Testing different stellar parameters.
Lee (2020)	Not explicitly discussed	Yes, double CN-CH anti-correlations on the RGB	Found five stellar populations.
Mészáros et al. (2020)	No	Sample too small to confirm Ca spread. No stars to confirm Ce or Nd spreads	20 stars with a $S/N > 70$ from the APOGEE survey.
This work	Yes, >0.24 dex	Yes	6 stars, strictly differential analysis.

Table 2. Line list for our target stars and reference star (NGC 6752-mg9). The digits to the left of the decimal point in the ‘Species’ column are the atomic number. The digit to the right of the decimal point is the ionization state (‘0’ = neutral, ‘1’ = singly ionized). See the associated publications for the original references for each log gf values. The full table is available as supplementary material. A portion is shown here for guidance regarding its form and content.

Wavelength (Å)	Species	L.E.P. (eV)	log gf	C (mÅ)	III-3 (mÅ)	III-14 (mÅ)	III-15 (mÅ)	III-52 (mÅ)	IV-102 (mÅ)	NGC 6752-mg9 (mÅ)
5682.63	11.0	2.1	-0.71	103.48	59.34	37.85	71.79	59.88	39.58	57.84
5688.2	11.0	2.1	-0.41		84.32	63.09	102.71	89.66	60.30	83.02
6160.747	11.0	2.1	-1.25	59.43	28.83	13.78	15.42	27.97	11.96	25.82
5711.09	12.0	4.34	-1.72	112.30	100.61	85.13	74.63	100.31	78.70	85.74
6698.673	13.0	3.14	-1.65	34.86	15.33	7.78	20.47	14.13	8.10	17.31

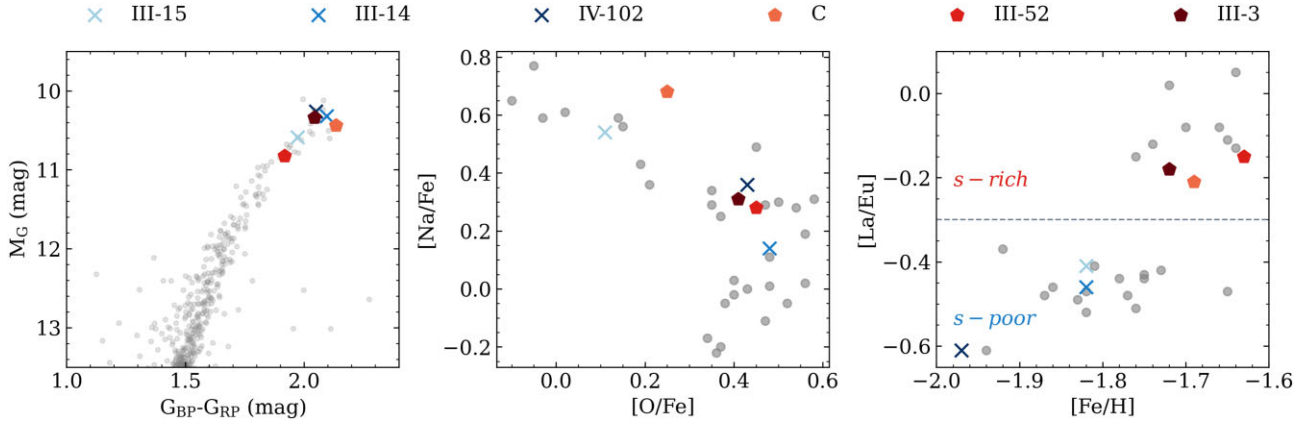


Figure 1. In each panel, we show our s -process poor stars in blue crosses (III-15, III-14, and IV-102) and s -process rich stars in red pentagons (C, III-52, and III-3). *Left-hand panel:* the RGB in M 22 using Gaia filters. All targets appear at the tip of the RGB. *Middle panel:* the Na-O anticorrelation using the sample of stars from Marino et al. (2011). Our stars span the range of the anticorrelation. There is no distinction in light element abundances between the two s -process groups. *Right-hand panel:* the division at $[La/Eu] = -0.3$ between s -process rich (top) and s -process poor (bottom) stars, as given in Marino et al. (2011).

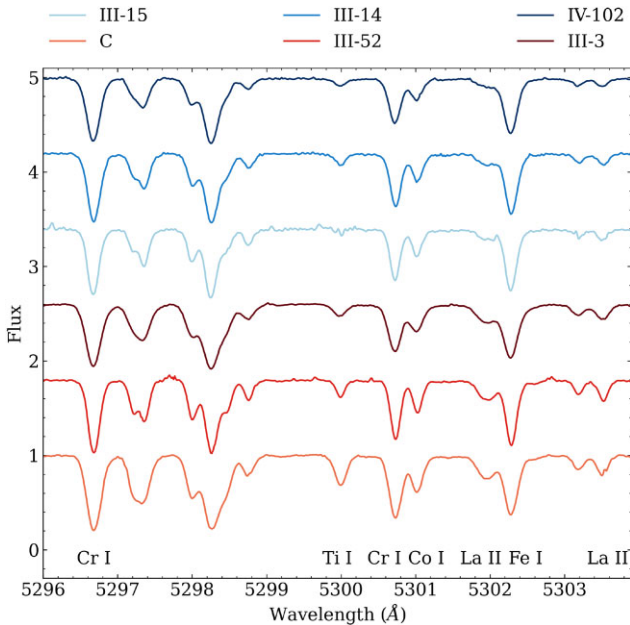


Figure 2. High signal-to-noise spectra of our target stars. Spectra increase in metallicity from the s -process poor stars in blue at the top to the s -process rich stars in red at the bottom. The blended regions from 5297 to 5299 Å are a combination of Cr I, Ti I, and Fe I. The s -process element La increases in strength from top to bottom as the metallicity increases.

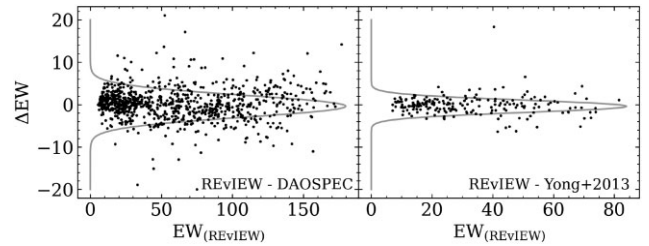


Figure 3. Comparison of EWs measured using DAOSPEC and with IRAF from Yong et al. (2013). The left-hand panel shows all lines measured ($N = 872$) using DAOSPEC for our program stars and the right-hand panel compares EW measurements for our reference star ($N = 199$). Overlaid is a Gaussian fit to the distribution and we find that compared to DAOSPEC, $\mu = 0.13$ mÅ, and $\sigma = 3.6$ mÅ and for Yong et al. (2013); $\mu = -0.12$ mÅ and $\sigma = 2.2$ mÅ.

Pancino 2008) for our program stars, and compare our measurements of our reference star with Yong et al. (2013). From Fig. 3, our method is in good agreement with both DAOSPEC and manual measurements using IRAF in Yong et al. (2013). As we have not manually removed poorly fit lines for this sample, EWs used to calculate abundances would be even more accurate than what each panel indicates. The advantages of our boutique method is that (i) the fitting process is much faster than IRAF, (ii) we inspect each line by eye to ensure that the continuum has been fit correctly, and (iii) we can remove blended lines or lines in low signal-to-noise regions. This is essential to remove spurious measurements in order to achieve extremely precise EW measurements.

Table 3. Stellar parameters and associated errors for our program stars. These stellar parameters are determined with respect to our reference star NGC 6752-mg9. For this star, we use the values from table 1 of Yong et al. (2013); $T_{\text{eff}} = 4288$ K, $\log g = 0.91$ dex, $[\text{Fe}/\text{H}] = -1.66$ dex, and $\xi = 1.72$ km s $^{-1}$. We also include whether a star belongs to the *s*-process rich group here for convenience.

Star	T_{eff} (K)	\pm (K)	$\log g$ (cm s $^{-2}$)	\pm (cm s $^{-2}$)	[Fe/H]	\pm	ξ (km s $^{-1}$)	\pm (km s $^{-1}$)	<i>s</i> -process rich?
C	3912	12	0.105	0.056	-1.696	0.013	2.08	0.03	✓
III-3	4041	14	0.250	0.064	-1.778	0.013	2.29	0.04	✓
III-14	4038	10	0.120	0.034	-1.87	0.011	2.24	0.03	×
III-15	4136	7	0.450	0.052	-1.825	0.010	2.03	0.02	×
III-52	4100	10	0.510	0.036	-1.707	0.010	1.93	0.02	✓
IV-102	4043	11	0.100	0.046	-1.973	0.014	2.43	0.03	×

Strong lines located in the flat part of the curve of growth have been excluded as their EWs are sensitive to the microturbulent velocity. We conservatively set this threshold to be 120 mÅ. Additionally, weak lines less than 5 mÅ have also been excluded due to larger fractional uncertainties.

2.3 Differential stellar parameters

To calculate our stellar parameters, we used the program q^2 as detailed in Ramírez et al. (2014). This code serves as a wrapper for the 1D local thermodynamic equilibrium (LTE) stellar line analysis program MOOG (Snedden 1973). q^2 applies a strictly differential line-by-line analysis between the program stars and a reference star by iterating over the stellar parameters in order to simultaneously minimize any correlations between (i) Fe I abundance and excitation potential χ , (ii) Fe I abundance and the reduced EWs ($\log(\text{EW}/\lambda)$), and (iii) removing any abundance difference between neutral (Fe I) and singly ionized iron (Fe II). Hence q^2 imposes excitation and ionization balance using the abundance differences between the program stars and reference star. That is, while the absolute abundances for Fe in a given star do not necessarily achieve excitation or ionization equilibrium, the abundance differences simultaneously satisfy excitation and ionization balance.

The model atmospheres used in the analysis were the one dimensional, plane-parallel, α enhanced, $[\alpha/\text{Fe}] = +0.4$, NEWODF grid of ATLAS9 models by Castelli & Kurucz (2003). Other studies have shown that MARCS models yield essentially identical results to the Castelli/Kurucz models (Alves-Brito et al. 2010). Literature values from Marino et al. (2011) were used as our initial stellar parameters and we discuss the impact on our choice of reference star and initial parameters in Section 4.1.1. For our reference star, we used NGC 6752-mg9 from Yong et al. (2013). This star's parameters have been estimated using photometric T_{eff} and $\log g$ from isochrones which has been recommended by studies such as Mucciarelli & Bonifacio (2020). These parameters are $T_{\text{eff}} = 4288$ K, $\log g = 0.91$ cm s $^{-2}$, $[\text{Fe}/\text{H}] = -1.66$ and $\xi = 1.72$ km s $^{-2}$.

We first perform one iteration of excitation/ionization balance through q^2 , and then remove all Fe I lines more than 1σ from the mean. We then re-run q^2 with this new subset of lines to obtain our final stellar parameters that are presented in Table 3 with their associated errors. In Table C1, we compare stellar parameters in the literature to our current work and find that our values are consistent with previous estimations. Although these stellar parameters are considered 'spectroscopic parameters', the differential nature of the analysis means that our program stars' iron abundances are measured with respect to our reference star on a line-by-line basis. Strict

differential analysis minimizes the impact of model uncertainties as well as errors in atomic data as they cancel-out in each line. We further note that high precision differential analyses deliver precise relative abundances. Such analyses have provided key breakthroughs for a range of objects including solar twins, open clusters, GCs, and halo stars (e.g. Meléndez et al. 2009; Yong et al. 2013; Liu et al. 2016; Reggiani et al. 2017; Bedell et al. 2018). Our average errors in stellar parameters across our target stars are $T_{\text{eff}} \pm 10.6$ K, $\log g \pm 0.048$ dex, $[\text{Fe}/\text{H}] \pm 0.012$ dex, and $\xi \pm 0.03$ km s $^{-1}$. These are significantly lower than traditional approaches (e.g. the lowest errors given in Marino et al. 2011 are $T_{\text{eff}} = 50$ K and $\log g = 0.14$) and comparable to other differential studies; stars with similar stellar parameters in Yong et al. (2013) have errors of $T_{\text{eff}} \approx 20$ K with $\log g = 0.01$ dex. In Section 4.1.2, we discuss the outcomes of using different reference stars and guess stellar parameters.

It is known that the abundance inferred from Fe I lines suffer from non-LTE (NLTE) effects (e.g. Thévenin & Idiart 1999; Kraft & Ivans 2003; Lee, Carney & Habgood 2005; Lee 2016), which may influence the traditional spectroscopic stellar parameter determinations. Our differential approach also minimises the impact of NLTE corrections as our reference star NGC 6752-mg9 is also an RGB tip star at a comparable temperature, gravity, and metallicity to our target stars. Therefore, only differential NLTE corrections are relevant, i.e. how much does the NLTE correction change as $[\text{Fe}/\text{H}]$ moves from -1.66 dex (reference) to -1.94 dex (most metal poor star). Similarly for T_{eff} , the differences in the NLTE corrections from 4288 K (reference) to 3937 K (coolest star) are relevant. We provide examples of this differential NLTE correction in Section 4.1.1.

The determination of stellar parameters for metal poor giants has been debated in the literature. Mucciarelli & Bonifacio (2020) recently discussed the influence when adopting spectroscopic parameters for stars with $[\text{Fe}/\text{H}] < -1.5$ dex. They flag that the photometric parameters agree with best-fitting stellar isochrones and thus are a more suitable choice of parameters for metal poor giants. As M 22 falls within this region, we justify our choice of stellar parameters in Section 4.1.1. While we would like to determine effective temperatures for our program stars using a photometric approach, differential reddening makes this problematic (see Crocker 1988, Monaco et al. 2004 and Alves-Brito et al. 2012 for reddening in the direction of M 22). Alternative photometric methods such as the infrared flux method do not achieve the required precision needed for ~ 0.01 dex errors on our abundances (e.g. Ramírez & Meléndez 2005). We also note that while Frebel et al. (2013) address the issue of reconciling spectroscopic and photometric temperature scales, their analysis was applied in the regime $-3.3 < [\text{Fe}/\text{H}] < -2.5$ which is more metal poor than M 22.

Table 4. Differential chemical abundances and their associated errors as evaluated by q^2 when using the reference star NGC 6752-mg9. # represents the number of lines used to calculate the abundance. The columns $\langle\Delta^X\rangle$ and $\sigma\langle\Delta^X\rangle$ represent the average and standard deviation across all stars, respectively. $\langle s\text{-poor}\rangle$ and $\langle s\text{-rich}\rangle$ are the average abundances divided based on their s -process group with $\sigma_{s\text{-poor}}$ and $\sigma_{s\text{-rich}}$ as their accompanying standard deviations. Finally $\langle s\text{-rich}\rangle - \langle s\text{-poor}\rangle$ is the differences between the two s -process groups.

	C	III-3	III-14	III-15	III-52	IV-102	$\langle\Delta^X\rangle$	$\sigma\langle\Delta^X\rangle$	$\langle s\text{-poor}\rangle$	$\sigma_{s\text{-poor}}$	$\langle s\text{-rich}\rangle$	$\sigma_{s\text{-rich}}$	$\langle s\text{-poor}\rangle - \langle s\text{-rich}\rangle$
Δ^{FeI}	-0.033	-0.106	-0.183	-0.147	-0.049	-0.268	-0.131	0.088	-0.199	0.062	-0.063	0.038	0.137
\pm	0.010	0.018	0.014	0.012	0.011	0.018							
#	99	111	112	114	120	102							
Δ^{FeII}	-0.019	-0.102	-0.179	-0.143	-0.041	-0.268	-0.125	0.092	-0.197	0.064	-0.054	0.043	0.143
\pm	0.040	0.030	0.025	0.021	0.025	0.028							
#	15	16	16	17	16	16							
Δ^{NaI}	0.315	-0.140	-0.417	0.000	-0.077	-0.413	-0.122	0.276	-0.277	0.240	0.033	0.247	0.309
\pm	0.059	0.035	0.017	0.172	0.017	0.043							
#	2	3	3	3	3	3							
Δ^{SiII}	0.118	0.077	-0.145	-0.144	0.037	-0.223	-0.047	0.141	-0.171	0.045	0.077	0.041	0.248
\pm	0.035	0.042	0.021	0.022	0.034	0.033							
#	10	11	11	11	11	11							
Δ^{CaI}	0.044	-0.121	-0.262	-0.190	0.042	-0.343	-0.138	0.159	-0.265	0.077	-0.012	0.095	0.253
\pm	0.029	0.031	0.026	0.021	0.022	0.028							
#	10	17	20	20	17	21							
Δ^{ScII}	-0.097	-0.137	-0.230	-0.113	-0.120	-0.227	-0.154	0.059	-0.190	0.067	-0.118	0.020	0.072
\pm	0.065	0.070	0.028	0.052	0.053	0.033							
#	3	3	3	3	3	3							
Δ^{TiI}	0.163	-0.033	-0.142	-0.134	0.081	-0.235	-0.050	0.150	-0.170	0.056	0.070	0.098	0.241
\pm	0.039	0.042	0.032	0.026	0.028	0.030							
#	28	34	35	44	34	35							
Δ^{TiII}	0.119	0.032	-0.133	-0.124	0.022	-0.180	-0.044	0.118	-0.146	0.030	0.058	0.053	0.203
\pm	0.061	0.061	0.033	0.034	0.041	0.040							
#	11	11	14	14	13	13							
Δ^{CrI}	0.092	-0.090	-0.161	-0.166	0.036	-0.250	-0.090	0.131	-0.192	0.050	0.013	0.093	0.205
\pm	0.058	0.060	0.060	0.054	0.072	0.057							
#	5	6	7	8	7	7							
Δ^{CrII}	0.305	0.090	-0.080	-0.100	0.075	-0.150	0.023	0.169	-0.110	0.036	0.157	0.129	0.267
\pm	0.176	0.018	0.090	0.110	0.106	0.051							
#	2	2	2	2	2	2							
Δ^{MnI}	0.040	-0.060	-0.145	-0.130	0.000	-0.330	-0.104	0.132	-0.202	0.111	-0.007	0.050	0.195
\pm	0.024	0.047	0.023	0.042	0.082	0.027							
#	1	2	2	2	2	2							
Δ^{CoI}	-0.020	-0.105	-0.225	-0.140	-0.030	-0.365	-0.148	0.131	-0.243	0.114	-0.052	0.046	0.192
\pm	0.000	0.035	0.045	0.010	0.030	0.095							
#	1	2	2	2	2	2							
Δ^{NiI}	0.081	-0.033	-0.170	-0.130	-0.017	-0.249	-0.086	0.119	-0.183	0.061	0.010	0.062	0.193
\pm	0.036	0.023	0.019	0.016	0.015	0.023							
#	38	40	41	42	42	42							
Δ^{ZnI}	0.110	0.330	-0.070	-0.170	0.040	-0.260	-0.003	0.212	-0.167	0.095	0.160	0.151	0.327
\pm	0.023	0.023	0.015	0.015	0.014	0.015							
#	1	1	1	1	1	1							

2.4 Chemical abundances

Having computed our stellar parameters using a strictly differential technique, q^2 then calculates abundances for Fe, Na, Si, Ca, Sc, Ti, Cr, Mn, Co, Ni, Zn, Y, Zr, La, Ce, Nd, Sm, and Eu in every program star using EWs measured with REVIEW. We adopt the notation from Meléndez et al. (2012) where the abundance difference (program star–reference star) for a line is given by

$$\delta A_i = A_i^{\text{program star}} - A_i^{\text{reference star}}.$$

For a given species X, the average abundance difference is

$$\langle\delta A_i^X\rangle = \frac{1}{N} \sum_{i=1}^N \delta A_i^X = \Delta^X,$$

where N is the number of lines, which we write as Δ^X . These abundances are provided in Tables 4 and 5. We stress that these abundances are with respect to our reference star NGC 6752-mg9 from Yong et al. (2013). We also compute these abundances on an absolute scale using the values given in table 5 of Yong et al. (2013). We find that our values are in good agreement with those from Marino

Table 5. An extension of Table 4 but for s and r -process elements.

	C	III-3	III-14	III-15	III-52	IV-102	$\langle \Delta^X \rangle$	$\sigma \langle \Delta^X \rangle$	$\langle s\text{-poor} \rangle$	$\sigma_{s\text{-poor}}$	$\langle s\text{-rich} \rangle$	$\sigma_{s\text{-rich}}$	$\langle s\text{-poor} \rangle - \langle s\text{-rich} \rangle$
Δ^{YII}	0.251	0.257	-0.326	-0.232	0.211	-0.420	-0.043	0.316	-0.326	0.094	0.240	0.025	0.566
\pm	0.048	0.075	0.028	0.028	0.034	0.040							
#	8	7	9	9	9	9							
Δ^{ZrII}	0.140	0.250	-0.230	-0.400	0.140	-0.380	-0.080	0.290	-0.337	0.093	0.177	0.064	0.513
\pm	0.012	0.012	0.009	0.010	0.012	0.009							
#	1	1	1	1	1	1							
Δ^{LaII}	0.092	0.060	-0.347	-0.255	0.150	-0.505	-0.134	0.271	-0.369	0.126	0.101	0.046	0.470
\pm	0.043	0.043	0.025	0.022	0.028	0.037							
#	6	6	6	6	6	6							
Δ^{CeII}	0.290	0.117	-0.307	-0.193	0.217	-0.460	-0.056	0.306	-0.320	0.134	0.208	0.087	0.528
\pm	0.130	0.017	0.013	0.143	0.012	0.027							
#	3	3	3	3	3	3							
Δ^{NdII}	0.294	0.137	-0.131	-0.116	0.195	-0.308	0.012	0.231	-0.185	0.107	0.209	0.079	0.394
\pm	0.050	0.040	0.035	0.031	0.025	0.032							
#	12	13	14	14	13	13							
Δ^{SmII}	0.180	0.310	-0.050	0.030	0.100	-0.270	0.050	0.200	-0.097	0.155	0.197	0.106	0.293
\pm	0.011	0.015	0.007	0.010	0.011	0.009							
#	1	1	1	1	1	1							
Δ^{EuII}	-0.100	-0.080	-0.150	-0.070	-0.080	-0.300	-0.130	0.088	-0.173	0.117	-0.087	0.012	0.087
\pm	0.021	0.020	0.010	0.016	0.015	0.020							
#	1	1	1	1	1	1							

et al. (2011), with an average difference in abundance between the two studies of ≈ 0.015 dex. We find larger variations for the s -process elements with a maximum difference of 0.14 dex between our values and abundances from Marino et al. (2011).

Tables 4 and 5 also provide the errors on these abundance measurements. q^2 computes errors by adding the line-to-line scatter in quadrature with the abundance errors propagated from the stellar parameters. With an average [Fe I/H] error of 0.014, our analysis is a factor of 10 more precise when compared to stars from Marino et al. (2011) with similar stellar parameters.

3 RESULTS

3.1 Differences between s -process groups

We reproduce the divide between the two s -process groups using $\Delta^{\text{La-Eu}}$ as a function of Δ^{Fe} in Fig. 4 (where these two values are analogous to [La/Eu] and [Fe/H] in square bracket notation, respectively). As in Marino et al. (2011), we see a clear separation in our program stars and find that there must be at least a 0.24 dex iron abundance spread in the cluster as well as a spread of at least 0.38 dex for $\Delta^{\text{La-Eu}}$. The mean iron abundance difference between the two populations is 0.14 dex. This is in very good agreement with Marino et al. (2011) who found a difference of 0.39 dex in [La/Eu], and a mean abundance difference of 0.15 dex in Fe (see the right-hand panel of Fig. 1). Therefore, we confirm the results from Lee (2016), Marino et al. (2011), Roederer et al. (2011), Da Costa et al. (2009), and several others that this is an anomalous stellar system with heavy element abundance variations.

Tables 4 and 5 list the mean abundance and dispersion in each s -process group for each element, along with the average difference between each group (i.e. $\langle s\text{-rich} \rangle - \langle s\text{-poor} \rangle$). These quantities are presented in Fig. 5 with elements colour-coded by their main nucleosynthesis sites. In the top panel, the blue crosses and red pentagons represent the dispersion of the s -process poor and rich

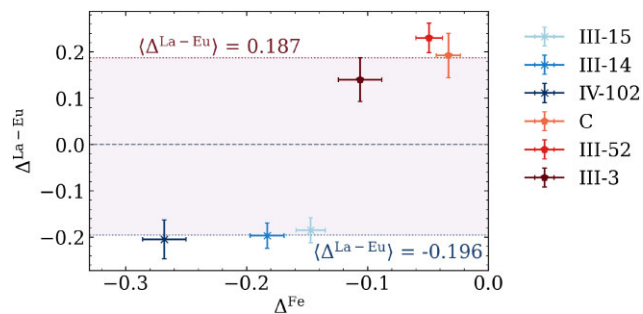


Figure 4. The $\Delta^{\text{La-Eu}}$ abundances as a function of Δ^{Fe} (analogous to [La/Eu] and [Fe/H] in square bracket notation, respectively). Using high precision differential abundance measurements, we still recover the split between the two s -process populations of stars. The horizontal dashed line in grey represents the $\Delta^{\text{La-Eu}}$ of the reference star and the horizontal blue and red lines are the average values of $\Delta^{\text{La-Eu}}$ for the s -process poor and rich groups, respectively. These results are in very good agreement with Marino et al. (2011).

populations, respectively. For our α -elements, each population has roughly the same dispersion with Na showing the largest spread overall due to light-element abundance variations within the cluster (as expected given the middle panel of Fig. 1). Iron peak elements show a mix of different dispersions, however, Fe in particular has a larger variation in its s -process poor population. Assuming this is the primordial population in the cluster, this could be a related phenomenon to the iron abundance spread in the first generation of stars observed in some Galactic GCs (e.g. Marino et al. 2019; Legnardi et al. 2022) and predicted by numerical simulations (McKenzie & Bekki 2021). For M 22, Fig. 5 also shows that all measured s -process elements have larger spread in the s -process poor populations, and the magnitude of these variations increases with atomic number.

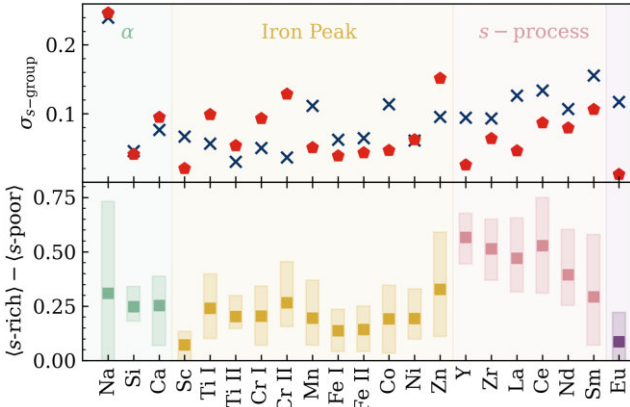


Figure 5. Comparing the different abundance variations within each s -process group. α -elements are shown in green, iron peak elements in yellow, s -process elements in pink, and our r -process element, Eu, in purple. *Top panel:* the 1σ dispersion for the s -process poor group in blue crosses, and the s -process rich group in red pentagons. The s -process poor population has a higher dispersion across all measured s and r -process elements. *Bottom panel:* the difference in abundances between the average s -process poor ($s - \text{poor}$) and s -process rich ($s - \text{rich}$) populations for each measured element. The shaded rectangle for each element represents the minimum and maximum abundance differences between the two populations, and square denotes the average difference between the two stellar groups ($|(s - \text{poor}) - (s - \text{rich})|$) in Tables 4 and 5. The shaded rectangles for Na, Sc, and Eu have overlapping abundances for the two populations so we crop their rectangles at 0.

In the bottom panel, the solid square is the mean difference between the two s -process groups and the shaded boxes are a representative of the minimum and maximum range of abundances within the cluster. For Na, Sc, and Eu, abundances between the two populations overlap with one another, therefore we set the minimum variation to 0. For the α and iron peak elements, there is an average abundance difference of ≈ 0.2 dex. For the s -process elements, however, as the atomic number increases, the mean separation decreases, but the total range in abundances increases. On average, there is a ≈ 0.5 dex difference and Y shows the largest spread between the two populations with a separation of almost 0.6 dex. These anomalous abundances represent a complex formation history and provide additional constraints to pin point the neutron sources and/or combination of neutron sources that are responsible for these differences.

We emphasize, however, that these results are limited by our small sample size and may not be a true reflection of the abundance differences within the cluster.

3.2 Chemical correlations

To further examine whether or not M 22 is indeed an anomalous cluster, we take a sample of elements each representing different nucleosynthetic processes and astrophysical sources and plot them in Fig. 6. On the y -axis, we use y to represent a first peak s -process element from AGB stars, Nd to represent second-peak elements, and Eu to represent elements made by the r -process. For the x -axis, Si is a proxy for alpha elements while Fe and Zn are our examples of iron-peak elements (Kobayashi et al. 2020). Although Fe and Zn trace similar nucleosynthesis sites, Zn is produced in high-energy explosions, more so than Fe. Additionally, Fe is also made in larger quantities in Type Ia supernovae compared to Zn.

For each element, we find abundance variations greater than the measurement uncertainty. The combination of Si-Y is particularly

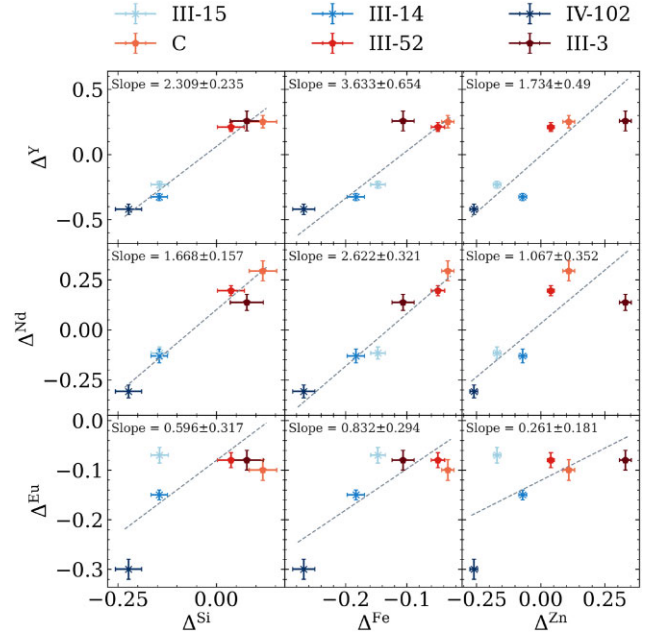


Figure 6. A grid of correlations between different elements. The Δ^X notation is analogous to $[X/H]$ in square bracket notation. On the y -axis, we include Y as a first s -process peak element, Nd as a second s -process peak element, and Eu as an r -process element. On the x -axis, we use Si as a proxy for alpha elements and both Fe and Zn as iron peak elements.

good for separating the two different s -process populations. There are no obvious correlations for the r -process element Eu. Additionally, it is unclear why the most metal poor star, IV-102, has an Eu abundance ~ 0.15 dex lower than the other program stars while still having very small abundance errors. The stellar parameters for this star are in good agreement with Marino et al. (2011; see Table C1), however, this may be an artefact of our differential approach with IV-102 being 0.3 dex more metal poor than our reference star. Eu can only be measured using the 6645 Å line that we manually inspected to ensure accurate EW fitting, and have included in Appendix B.

Taking only the linear fits from Fig. 6 and applying this method to a larger sample of elements, Fig. 7 illustrates the correlations between all the elements with the significance of its correlation colouring each axis. This serves as a comparison to figs 16, 17, 19, and 20 presented in Yong et al. (2013) and bears some similarity to the RGB bump sample used in this work. We select only elements that were measured using at least two lines. The tight correlation between Y and Si is illustrated here by $\approx 10\sigma$ significance. Na has correlations with lower statistical significance compared to other elements, which is a result of the light element abundance variations within the cluster. As expected, we see the s -process elements Y, La, and Nd strongly correlate with each other.

4 DISCUSSION

4.1 An abundance spread in M 22?

As evident from Table 1, the debate as to whether M 22 has a range in heavy element abundance has swung back and forth due to a number of divergent results. A recent work reporting no iron spread in the cluster from Mucciarelli et al. (2015) was a prominent factor in Pfeffer et al. (2021), rejecting M 22 as a nuclear star cluster (NSC). Our study has the highest resolution and S/N data ever taken of M

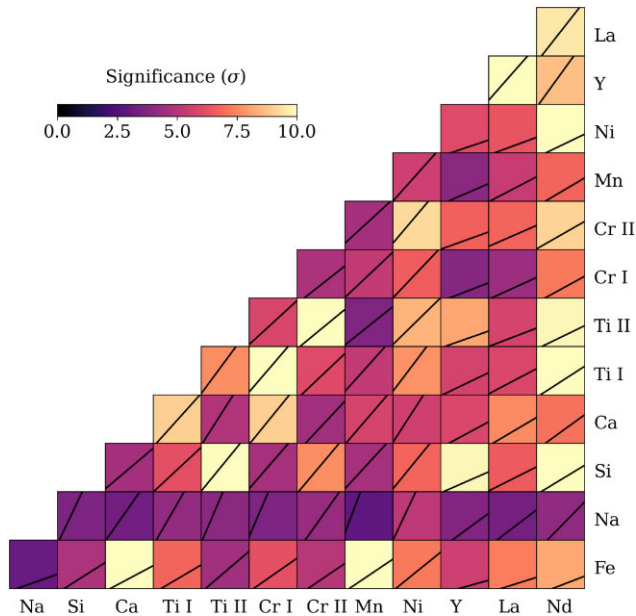


Figure 7. Linear fit to Δ^X versus Δ^Y (as in Fig. 6), for a subset of elements measured with at least three lines. The plots along the x and y-axis all share the same plot ranges. The significance of the gradients is indicated by the colour bar. For example, Na has a less significant correlation between other elements compared to Nd.

22 stars, allowing us to provide a definitive answer to the question of whether M 22 contains significant abundance variations.

Norris, Ryan & Beers (2001) introduced a ‘figure of merit’ (F) for spectra; $F = R \times S/N / \lambda$, where R = spectral resolution, S/N = signal-to-noise ratio, and λ = wavelength. The most popular spectroscopic data set of M 22 comes from Marino et al. (2009), which has a wavelength range 4800–6800 Å, a resolution $R \simeq 45\,000$, and a typical S/N between 100 and 120, thus resulting in $F = 1058$ at $\lambda = 5100$ Å. This is a factor of six lower than our data that has $R = 110\,000$ and has $S/N = 300$ at 5100 Å, giving $F = 6470$. Furthermore, the high-quality EW measurements and differential analysis approach employed in for this work, using q^2 enables typical relative abundance errors of 0.01 dex, and is a proven method to deliver the highest possible precision (Nissen & Gustafsson 2018). Yong et al. (2013) applied this method to NGC 6752, a cluster with previously no evidence of an *s*-process or Fe abundance variations, and uncovered Fe spreads of ~ 0.02 – 0.03 dex. This makes our study extremely well-suited to discussing the intricacies of determining whether M 22 contains a genuine heavy abundance spread.

4.1.1 Determination of stellar parameters

Brown et al. (1990) stated that ‘Persistent but equivocal evidence of variable reddening in M 22 has confused efforts to ascertain the reality of an abundance spread in the cluster’. As evident from the extinction map in Alves-Brito et al. (2012), reddening presents a source of uncertainty for determining stellar parameters in M 22 through various photometric methods. However, Marino et al. (2011) emphasised that spectroscopic [Fe/H] measurements do not suffer the effects of differential reddening. Conclusions from Mucciarelli et al. (2015) act as a precursor to the discussion in Mucciarelli & Bonifacio (2020), which warn against using spectroscopic parameters at metallicities lower than -1.5 dex. They find that spectroscopic parameters are inconsistent with the position of the stars in the CMD,

thus resulting in an underestimate of the temperatures and gravities. Regarding the use of isochrones for this type of investigation, we note that Joyce & Chaboyer (2018) provide a detailed discussion of the uncertainties in the input physics for theoretical stellar evolution models and note that careful considerations and analysis need to be taken into account. By using photometric or spectroscopic T_{eff} and a photometric $\log g$, Mucciarelli et al. (2015) reported no abundance spread in M 22, finding a narrow, symmetric [Fe II/H] distribution with a value of -1.75 ± 0.01 dex. They also analysed stars in NGC 6572 from Yong et al. (2013), including the reference star used in this work, and found a unimodal distribution for all methods of determining parameters. However, Fabiola Marino (2015) discusses this work in the context of C + N + O abundance differences between the two populations. When plotting the stellar parameters from Mucciarelli et al. (2015) with isochrones, which account for the CNO variations, the $\log g$ values are systematically affected, but not to the same degree for the two populations; the *s*-poor population to have systematically higher $\log g$.

Lee (2016) provides a comprehensive discussion of the results from Mucciarelli et al. (2015), echoing the conclusion from Marino (2015) that that incorrect surface gravities were likely used. Additionally, the metallicity of the input atmosphere models and the separation in Fe II can be amplified if different methods are used to compute these parameters. Other studies have cited that the discrepancies between different methods have been attributed to non-LTE (NLTE) effects. Lind, Bergemann & Asplund (2012) presents a detailed discussion of the influence of NLTE on Fe, and by extension, the impact it has on stellar parameters. They explain that the metallicity of a star is primarily based on Fe I lines, which are far less sensitive to surface gravity variations compared to Fe II lines. However, these lines are subject to significant NLTE effects and the LTE ionization balance is not always realistic, resulting in an underestimation of surface gravity and metallicity. Comparing our results to previous parameters in the literature in Table C1, the $\log g$ determined in our study are indeed lower than other works (on the order of ~ 0.2 dex), however, our metallicities agree with previous estimates.

NLTE corrections for Fe are negligible for this work. Using corrections from Lind et al. (2012) and taking stellar parameters of program star III-3 from Mucciarelli et al. (2015; method 2) as an example ($T_{\text{eff}} = 3960\text{K}$, $\log g = 0.34$, [Fe/H] = -1.8), the NLTE corrections are ~ 0.01 dex using the closest matching parameters in their grid. Furthermore, as we are using a differential approach, it is the ‘differential NLTE’ corrections that will impact our abundances, which by design, will also be negligible. Taking a sample of Fe lines from the inspect data base³ (Bergemann et al. 2012; Lind et al. 2012), the difference in NLTE correction corrections between the reference and our most metal poor star, IV-102, was on the order of 0.001 dex.

4.1.2 Choice of reference star

Mucciarelli & Bonifacio (2020) cite inadequacies of the adopted physics, in particular the assumption of 1D geometry, can be the origin of the diverging spectroscopic and photometric parameters. As we have shown in previous sections, our approach of using differential measurements addresses this concern as this method aims to minimize errors arising from 1D models between the program and reference stars (for a review on differential methods, see Nissen & Gustafsson 2018).

³Data obtained from the INSPECT data base, version 1.0 (www.inspect-star.s.net).

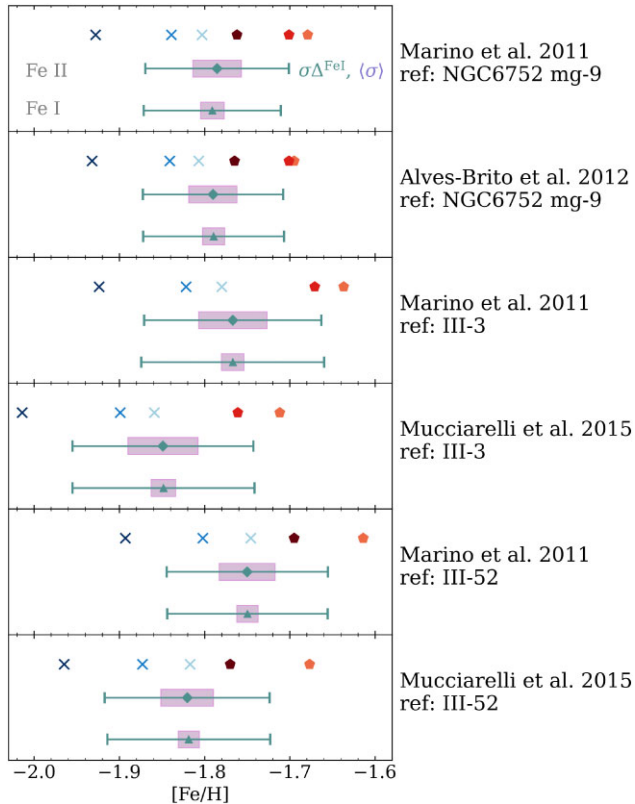


Figure 8. Each panel illustrates the spread in Fe, given different initial values from the literature, and different reference stars. The Fe II abundances are shown at the top of every panel, with the same colours and markers used in Figs 4 and 6. For both Fe I and Fe II abundances, the green error bar represents the 1σ standard deviation of Fe for our program stars and the purple box on top of it is the average error for each of the stars. Fe I and Fe II abundances are almost identical (as q^2 has imposed ionisation balance), however, Fe I has smaller errors for each star (i.e. smaller purple error bars) as more lines are measured. The results presented in this paper are from the top panel that uses stellar parameters from Marino et al. (2011) as starting values for the program stars with NGC 6752 mg-9 as the reference star.

We test the impact of different stellar parameters on iron abundances in Fig. 8. The text to the left of each panel describes the initial values and reference star used for abundance determinations. The top panel reflects abundances presented in this work, using the stellar parameters from Marino et al. (2011) as starting values and the reference star, NGC 6752 mg-9, from Yong et al. (2013). Additional models use Alves-Brito et al. (2012) initial values for the program stars [except for the C star which uses Marino et al. (2011) values] with NGC 6752 mg-9 as the reference, Marino et al. (2011) initial values with III-3 as the reference, Marino et al. (2011) initial values for the program stars with Mucciarelli et al. (2015) initial values for III-3 as the reference, all Marino et al. (2011) initial values with III-52 as the reference, and Marino et al. (2011) initial values for the program stars with Mucciarelli et al. (2015) values for III-52 as the reference. In all panels, the abundances have been scaled by the metallicity of the reference star in order for each measurement to be in the same Fe range. However, [Fe/H] abundances should not be compared between methods. If there was no abundance spread within M 22, we would expect that the green error bars of the Fe abundances would be the same length as the purple rectangles showing the size of the errors. However, regardless of the model, the stellar parameters

always converge on a sample of stars with an Fe spread (both Fe I and Fe II) greater than the errors expected for each star. Each iteration of determining stellar parameters arrives at slightly different stellar parameters, depending on the reference star and the initial values provided. This is unsurprising as the documentation for q^2 explains that the final stellar parameters will be somewhat dependent on the initial parameters and parameter steps. However, in each case, the scatter in Fe remains and the pattern between s -process rich and poor stars is retained. The abundances derived using different initial guesses and reference stars are in agreement with those found from the fiducial model.

We perform additional tests by selecting a reference star from the Gaia benchmark sample (Heiter et al. 2015). These stars have known radii, fluxes, and distances, which enable direct measurements of T_{eff} and $\log g$ from the Stefan–Boltzmann relation and Newton’s law of gravity, respectively (Heiter et al. 2015; Jofré et al. 2015). We analyse MIKE spectra of the Gaia benchmark metal-poor red giant star HD 122563 in the same way as our program stars. NLTE and 3D-NLTE stellar parameters from Bergemann et al. (2012) and Amarsi et al. (2016), respectively were adopted and the M 22 program stars were analysed using HD 122563 as the reference. We find the relative abundances between s -process poor and rich stars remains the same, but the errors are much larger due to the differences in parameters between HD 122563 and our reference and program stars (e.g. HD 122563 has [Fe/H] = -2.49 dex as compared to our most metal-rich star, C, with [Fe/H] = -1.68 dex).

4.1.3 Other non-detections

Previous non-detections of iron abundance spreads have been due to limited sample size (e.g. Cohen 1981), abundance errors being larger than the intrinsic spread (e.g. Anthony-Twarog et al. 1995) or techniques relating to the determination of stellar parameters (e.g. Mucciarelli et al. 2015). A study that does not suffer from these issues is from Mészáros et al. (2020), which analysed 20 stars with a $S/N > 70$ from the SDSS-IV APOGEE-2 survey. They estimate a higher [Fe/H] than previous studies for the cluster (-1.52 dex) with an average uncertainty of 0.09 dex. The Fe scatter is reported to be 0.112 dex, however, they say they cannot make strong statements about the intrinsic [Fe/H] scatter. Their results for the [Fe/H] scatter in ω Cen using 775 stars with a $S/N > 70$ are noticeably smaller than what is quoted in the literature; they detect a spread of 0.205 dex, whereas other studies report a value of a ~ 1.2 dex (e.g. Norris & Da Costa 1995; Johnson & Pilachowski 2010). Thus if the cluster with the largest heavy abundance variations known to date has a detected spread of 0.2 dex, then it is unsurprising that the ‘less extreme version’ of this cluster would have an undetectable spread given their analysis techniques. Horta et al. (2020) also used APOGEE abundances for M 22 in their work, but clipped around the [Fe/H] value from the 2010 edition of the Harris catalogue Harris (1996) to establish membership. Harris (1996) lists the metallicity of M 22 as [Fe/H] = -1.7 , so the sample would have been skewed towards the s -process rich population and it is understandable why no abundance spread was detected.

Photometric studies, such as Anthony-Twarog et al. (1995) or Monaco et al. (2004), allow for a maximum range in Fe abundance variations of ≈ 0.2 dex, comparable to the minimum allowable spread presented in this work. We note that these studies are affected by difficulties in ascertaining the reddening of the cluster and do not account for C + N + O differences between the two populations, which is estimated to be $\Delta[C + N + O] \approx 0.13$ dex (Marino et al.

2011).⁴ Theoretical works have shown that the T_{eff} of stars along the horizontal branch, as well as the mass-loss along the RGB is affected by the CNO abundance (Cassisi et al. 2008; Ventura et al. 2009), which may therefore influence photometric results.

4.2 The origin of M 22

Building an unambiguous evolutionary picture for a GC is a difficult task, even more so for a cluster with a surplus of anomalous observations. This work, among many others, has demonstrated the existence of abundance spreads for almost all elements in M 22. Historically, this has led many to believe that, like ω Cen, it is a probable nucleus of a stripped dwarf galaxy (Freeman 1993; Bekki & Freeman 2003). However, there is a disparity between its chemical and dynamical histories. Massari, Koppelman & Helmi (2019) used *Gaia* DR2 integrals of motion to assign GCs to accretion events to determine whether they are formed within the Milky Way (MW). Their results suggest that M 22 is a member of the MW disc. It is difficult to envision a scenario where a merging event with the MW can deposit a cluster on such a disc-like orbit, thus in light of this and our current understanding of the chemical and dynamical state of M 22, we discuss three possible formation scenarios. We intend on investigating M 22's creation through the lens of Mg isotope ratios in future works.

4.2.1 A nuclear star cluster?

There is historical precedence for M 22 to be labelled as a NSC. As discussed in Hesser et al. (1977), Lloyd Evans (1978b), and more recently in Da Costa et al. (2009), its similarities to ω Cen, especially in regards to its heavy element abundance spreads, indicate that these clusters share a similar origin. Furthering this claim, Da Costa (2016) discussed the theory that all clusters with substantial internal [Fe/H] spreads originated as nuclei of disrupted dwarf galaxies (for a recent review on NSCs, see Neumayer, Seth & Böker 2020). Recently, Pfeffer et al. (2021) claimed that metallicity variations, together with the extragalactic origin, are the requirements that a GC needs to be an NSC. Based on this hypothesis and the work from Mucciarelli et al. (2015) and Mészáros et al. (2020), they concluded that ‘M 22 is not likely to host significant spreads in [Fe/H], hence it is not a candidate NSC’. Our results, along with others listed in Table 1, provide strong evidence from a variety of approaches, for the existence of an iron spread. However, the dynamical history of this cluster does pose some challenges for this formation scenario. Recent work identifying the origin of ω Cen through its dynamical history strongly suggests an extragalactic formation site (Myeong et al. 2019), but M 22 does not share a similar history. In addition to Massari et al. (2019), Moreno et al. (2022) also lists M 22 as a main disc cluster, with orbital parameters largely in agreement with previous estimations in the literature (Gaia Collaboration 2018, Bajkova & Bobylev 2021 and the compilation by Holger Baumgardt⁵ using the Galactic Model I of Irrgang et al. 2013). Conversely, Callingham et al. (2022) assigns an 85 per cent probability of M 22, belonging to the Gaia–Enceladus–Sausage, as found by their chemodynamical model.

Horta et al. (2021a) discussed the presence of a low-metallicity accreted structure in the inner galaxy, however, M 22's orbital energy and eccentricity (based on values from Bajkova & Bobylev 2021) do

not fit these criteria. Recently, Santistevan et al. (2021) discussed the origin of metal-poor stars on prograde disc orbits using the FIRE-2 suite of cosmological zoom-in simulations. One of their findings was that a gas-rich merger could deposit a significant population of old metal-poor stars and gas into the host on the same orbital vector, which typically seeded/shaped the formation of a long-lived disc in the host. This resulted in metal-poor stars being preferentially on a prograde disc orbit. Future theoretical works should explore the possibility of a merging event at a low inclination to the disc depositing a GC with a disc-like orbit and with orbital energies and eccentricities similar to that of M 22. This would allow for the scenario where M 22 is an NSC. Furthermore, whether this accretion can occur before or after the MW disc has been established should also be investigated.

4.2.2 The product of two merged clusters?

ω Cen is not the only cluster that has frequently been compared to M 22. As discussed in Roederer et al. (2011), the heavy elements in NGC 1851 are reminiscent of the patterns observed in M 22. van den Bergh (1996) and Campbell et al. (2012) each discuss the possibility of merging clusters resulting in abundance spreads. Carretta et al. (2010b) supported this idea for NGC 1851, measuring a [Fe/H] spread of 0.06–0.08 dex. This has been further investigated by Tautvaisiene et al. (2022) who used the averaged $A(C + N + O)$ values to make the case that NGC 1851 is composed of two clusters. Because of the chemical parallels between M 22 and NGC 1851 (see Yong & Grundahl 2008; Yong et al. 2009; Carretta et al. 2011 for NGC 1851), one could assume that M 22 is also the result of two merging clusters. Corroborating this idea, Lee (2016) decomposed M 22 into five different populations, thus satisfying the conventional first-generation and second-generation patterns observed in Galactic GCs.

Simulations of an anomalous GC being created through a merging event were discussed in Bekki & Yong (2012) and Bekki & Tsujimoto (2016). They state that the merger must occur within a dwarf galaxy and the abundances of the resulting cluster can depend of the host galaxy's chemical evolution. In a galaxy with mass $\sim 10^{10} M_{\odot}$, two massive GCs ($> 3 \times 10^5 M_{\odot}$) can merge to form a single nucleus before its host is completely destroyed by an MW-like potential. A prediction of this scenario is that the resulting star cluster would be rotating and as such, M 22 has been confirmed to rotate by several studies (Bianchini et al. 2018; Gaia Collaboration et al. 2018; Sollima, Baumgardt & Hilker 2019; Vasiliev 2019; Vasiliev & Baumgardt 2021). Additionally, structural differences between enriched populations can be achieved by varying the densities of the two clusters (Gavagnin, Mapelli & Lake 2016). Khoperskov et al. (2018) and Mastrobuono-Battisti et al. (2019) conducted similar merging experiments but focused on clusters in the thick disc. They found that given a large, massive population of disc clusters, mergers, fly-bys, and mass exchanges between GCs can occur over time. They calculate that a single merger event can occur each Gyr given a population of ~ 100 GCs with initial masses of $10^7 M_{\odot}$ in a galactic disc, with a scale-length and height similar to the current MW thick disc. In the context of M 22, this scenario negates the requirement for an accretion event to place M 22 on a disc-like orbit while also generating abundance variations. Cluster merging is not frequent enough to account for the growing number of Type II clusters with common chemical patterns (e.g. metal-rich stars are enhanced in *s*-process elements and in their overall C + N + O abundances).

⁴Note that this study measured only an upper limit to the N abundance for almost all the *s*-poor stars, suggesting that the real difference could be larger.

⁵<https://people.smp.uq.edu.au/HolgerBaumgardt/globular/>

Despite both observational and theoretical support for this scenario, it is still unclear how the *s*-process rich population (in this case, a fully fledged GC prior to merging) acquired a surplus of these heavy elements in the first place. However, there are studies that have examined the role of AGBs in this scenario (Shingles et al. 2014; Straniero, Cristallo & Piersanti 2014). Furthermore, as in Fig. 6, the differences in abundances between the two populations varies depending on nucleosynthetic site amongst other factors. Variations within each individual *s*-process group (e.g. Δ^{FeI} variations of 0.06 and 0.04 dex for *s*-process rich and poor populations, respectively, in Fig. 5) also adds to the complexity of the scenario. How this chemical pattern can be established through a merging event is still an open question.

4.2.3 A building block of the Milky Way?

The stellar disc of the MW is a complex structure and its formation and evolution with regards to physical and dynamical processes continues to be debated (e.g. see Katz et al. 2021). Large spectroscopic surveys have begun to dissect the metal poor tail of the disc (Beers et al. 2002; Kordopatis et al. 2013; Li & Zhao 2017; Sestito et al. 2019; Di Matteo et al. 2020; Fernández-Alvar et al. 2021) and stars with kinematics akin to the thin and thick disc have been identified at metallicities ranging from $[\text{Fe}/\text{H}] = -6$ to -2 dex. Very recent work from Belokurov & Kravtsov (2022) presents the discovery of the original *in situ* component of the MW, dubbed *Aurora*. These low-metallicity ($[\text{Fe}/\text{H}] \lesssim -1.3$ dex) stars were born before any coherent disc was established and reflect the chaotic pre-disc period of the MW's evolution. Within this component, they identified a small fraction of stars with chemical correlations reminiscent of typical GCs. Hence, given M 22's metallicity range of $-2 \lesssim [\text{Fe}/\text{H}] \lesssim -1.6$ and disc-like kinematics, we suggest that this cluster could have formed alongside this metal-poor component and be a remnant of the building blocks of the MW. Furthermore, Myeong et al. (2022) determined that this component is enhanced in *s*-process elements, indicating a common but not necessarily shared nucleosynthetic history between *Aurora* and M 22. Thus, the assembly sequence of the MW could be encoded in the abundances of M 22 and be used to probe different nucleosynthesis processes during the earliest stage of our Galaxy's evolution.

The question of how M 22 survived the formation of the disc, and why it possesses such unusual chemical abundances remains unclear. The only other anomalous disc cluster as listed by Massari et al. (2019) is NGC 7078 (M15; e.g. Sneden et al. 1997; Sneden et al. 2000; Nardiello et al. 2018) and the rest of the GC population either has typical Type I GC abundance pattern or is too poorly studied to comment on. If there once were more M 22-like clusters, they have since dissolved and have not been identified. N-rich stars, usually the markers of dissipated GCs, are most commonly discussed in the context of the halo (Martell et al. 2011; Martell et al. 2016; Fernández-Trincado et al. 2017; Horta et al. 2021b) or the bulge (Schiavon et al. 2017; Bekki 2019; Fernández-Trincado et al. 2020) but rarely in the disc. Furthermore, a bimodal *s*-process element pattern is not apparent in the MW thick disc (e.g. Tautvaišienė et al. 2021).

A variation of the scenario commonly described for Type I GC formation could be adapted to the formation of M 22. In this scenario, GCs with two populations varying in light element abundances but not in heavy elements are formed through the ejecta of AGB stars, or a mixture of AGB ejecta and pristine gas with comparable abundances to the 1G (e.g. Cottrell & Da Costa 1981; D'Ercole et al. 2008;

Renzini et al. 2015; D'Antona et al. 2016). Within this framework, two possible scenarios emerge that could lead to the abundances of M 22. One could assume that the *s*-process poor population initially forms, then enriched AGB ejecta from these stars creates the *s*-process rich population. Two independent teams (Shingles et al. 2014; Straniero et al. 2014) examined this scenario and concluded that the *s*-process abundance differences between the two stellar groups can be attributed to pollution from AGB stars with masses in the range 3–6 M_{\odot} . Alternatively, accreted gas enriched in *s*-process elements could have also contributed to the *s*-rich population. In both cases, a contribution from supernovae is also necessary to reproduce the Fe enhancement in the *s*-process rich population of M 22. Further investigation into whether the light element variations can also be reproduced by this scenario is necessary.

Three theoretical works that illustrate this process include Calura et al. (2019), McKenzie & Bekki (2021), and Lacchin, Calura & Vesperini (2021). Each has had success in generating anomalous clusters that have a range in heavy element abundances.

Although this scenario can explain M 22's membership to the disc and has enough freedom in its formation scenario to explain the abundance patterns, the question of why this cluster is so unique when compared to the rest of the disc cluster population is something that requires further investigation.

5 CONCLUSIONS

The main result from our study is that high precision differential abundance measurements have not only verified the metallicity spread in the cluster M 22, but also variations in each of its *s*-process populations. The spectra analysed in this work are the highest quality ever obtained (in terms of spectral resolution and SNR), and the strictly differential nature of the analysis allows us to reach Fe uncertainties as low as ~ 0.01 dex. Hence, these are the most precise abundances ever obtained for this cluster. Our method addresses the concerns of NLTE calculations by using a well-characterised reference star to compare our observations to. We take a boutique approach for determining EWs by manually inspecting each line to honour and preserve the integrity of the data. The iron abundance spread persists even when using different reference stars and stellar parameters, determined both spectroscopically and photometrically. The iron spread (and *s*-process element spread) reported here is in good agreement to that of Marino et al. (2011); the difference being that the errors have been reduced by a factor of ~ 10 . We find that across all measured α and iron peak elements, there is an average difference of ≈ 0.2 dex between the two populations, and a ≈ 0.5 dex difference for the *s*-process elements. We find a positive correlation between all elements, with some combinations showing a bimodal separation, whereas others have a gradual transition between the two *s*-process groups. This data set will be used to further examine the AGB scenario by measuring isotopic ratios of Mg that we hope will put further constraints on possible formation mechanisms. There is no clear evolutionary scenario that can account for both the chemical abundances patterns as well as the dynamical history discussed in other works. For now, M 22 remains yet another enigma of our Galaxy.

ACKNOWLEDGEMENTS

The authors are grateful for the referee's thorough and fair assessment of this work. We thank both Dr Kenji Bekki for the useful discussions of M 22 in the context of simulations and Dr Thomas Nordlander

for his help in interpreting our differential stellar parameters and abundances in relation to NLTE effects.

MM is supported by the Australian Government Research Training Program (RTP) Scholarship.

This research was supported by the Australian Research Council Centre of Excellence for All Sky Astrophysics in 3 Dimensions (ASTRO 3D), through project number CE170100013.

IUR acknowledges support from the NASA Astrophysics Data Analysis Program (80NSSC21K0627), and the United States National Science Foundation (PHY 14-30152: Physics Frontier Center/JINA-CEE, AST 1613536, and AST 1815403/1815767).

This work has received funding from the European Research Council ((0:funding-source 3:href="http://dx.doi.org/10.13039/100106663")ERC/(0:funding-source)) under the European Union's Horizon 2020 research innovation programme (grant agreement ERC-StG 2016, No 716082 'GALFOR', PI: Milone, <http://progetti.dfa.unipd.it/GALFOR>), APM acknowledges support from MIUR through the FARE project R164RM93XW SEMPLICE (PI: Milone) and the PRIN program 2017Z2HSMF (PI: Bedin).

This research has made use of NASA's Astrophysics Data System and Bibliographic Services. This research has made use of the SIMBAD database, operated at CDS, Strasbourg, France. IRAF is distributed by the National Optical Astronomy Observatory, which is operated by the Association of Universities for Research in Astronomy (AURA) under a cooperative agreement with the National Science Foundation. This work has made use of data from the European Space Agency (ESA) mission *Gaia* (<https://www.cosmos.esa.int/gaia>), processed by the *Gaia* Data Processing and Analysis Consortium (DPAC, <https://www.cosmos.esa.int/web/gaia/dpac/consortium>). Funding for the DPAC has been provided by national institutions, in particular the institutions participating in the *Gaia* Multilateral Agreement. This research has made use of the AstroBetter blog and wiki.

DATA AVAILABILITY

Data are available from ESO website with program ID = '095.D-0027(A)'.

REFERENCES

Alves-Brito A., Meléndez J., Asplund M., Ramírez I., Yong D., 2010, *A&A*, 513, A35

Alves-Brito A., Yong D., Meléndez J., Vásquez S., Karakas A. I., 2012, *A&A*, 540, A3

Amarsi A. M., Lind K., Asplund M., Barklem P. S., Collet R., 2016, *MNRAS*, 463, 1518

Anthony-Twarog B. J., Twarog B. A., Craig J., 1995, *PASP*, 107, 32

Arp H. C., Melbourne W. G., 1959, *AJ*, 64, 28

Bajkova A. T., Bobylev V. V., 2021, *Res. Astron. Astrophys.*, 21, 173

Bastian N., Lardo C., 2018, *ARA&A*, 56, 83

Battaglia G., North P., Jablonka P., Shetrone M., Minniti D., Díaz M., Starkenburg E., Savoy M., 2017, *A&A*, 608, A145

Bedell M. et al., 2018, *ApJ*, 865, 68

Beers T. C., Drilling J. S., Rossi S., Chiba M., Rhee J., Führmeister B., Norris J. E., von Hippel T., 2002, *AJ*, 124, 931

Bekki K., 2019, *MNRAS*, 490, 4007

Bekki K., Freeman K. C., 2003, *MNRAS*, 346, L11

Bekki K., Tsujimoto T., 2016, *ApJ*, 831, 70

Bekki K., Yong D., 2012, *MNRAS*, 419, 2063

Belokurov V., Kravtsov A., 2022, *MNRAS*, 514, 689

Bergemann M., Lind K., Collet R., Magic Z., Asplund M., 2012, *MNRAS*, 427, 27

Bessell M. S., Norris J., 1976, *ApJ*, 208, 369

Bianchini P., Varri A. L., Bertin G., Zocchi A., 2013, *ApJ*, 772, 67

Bianchini P., van der Marel R. P., del Pino A., Watkins L. L., Bellini A., Fardal M. A., Libralato M., Sills A., 2018, *MNRAS*, 481, 2125

Bond H. E., 1975, *ApJ*, 202, L47

Brown J. A., Wallerstein G., 1992, *AJ*, 104, 1818

Brown J. A., Wallerstein G., Oke J. B., 1990, *AJ*, 100, 1561

Busso M., Gallino R., Wasserburg G. J., 1999, *ARA&A*, 37, 239

Butler D., Kraft R. P., Miller J. S., Robinson L. B., 1973, *ApJ*, 179, L73

Callingham T. M., Cautun M., Deason A. J., Frenk C. S., Grand R. J. J., Marinacci F., 2022, *MNRAS*, 513, 4107

Calura F., D'Ercole A., Vesperini E., Vanzella E., Sollima A., 2019, *MNRAS*, 489, 3269

Campbell S. W. et al., 2012, *ApJ*, 761, L2

Cannon R. D., 1980, *A&A*, 81, 379

Cannon R. D., Stobie R. S., 1973, *MNRAS*, 162, 207

Carretta E., Bragaglia A., Gratton R., D'Orazi V., Lucatello S., 2009, *A&A*, 508, 695

Carretta E. et al., 2010a, *A&A*, 520, A95

Carretta E. et al., 2010b, *ApJ*, 722, L1

Carretta E., Lucatello S., Gratton R. G., Bragaglia A., D'Orazi V., 2011, *A&A*, 533, A69

Carretta E. et al., 2013, *A&A*, 557, A138

Cassisi S., Salaris M., Pietrinferni A., Piotto G., Milone A. P., Bedin L. R., Anderson J., 2008, *ApJ*, 672, L115

Castelli F., Kurucz R. L., 2003, in Piskunov N., Weiss W. W., Gray D. F., eds, Proc. IAU Symp. Vol. 210, Modelling of Stellar Atmospheres, Poster Contributions. Astron. Soc. Pac., San Francisco, p. A20

Clayton D. D., Fowler W. A., Hull T. E., Zimmerman B. A., 1961, *Ann. Phys.*, 12, 331

Cohen J. G., 1981, *ApJ*, 247, 869

Cordoni G., Milone A. P., Mastrobuono-Battisti A., Marino A. F., Lagioia E. P., Tailo M., Baumgardt H., Hilker M., 2020a, *ApJ*, 889, 18

Cordoni G. et al., 2020b, *ApJ*, 898, 147

Cote P., Pryor C., McClure R. D., Fletcher J. M., Hesser J. E., 1996, *AJ*, 112, 574

Cottrell P. L., Da Costa G. S., 1981, *ApJ*, 245, L79

Crocker D. A., 1988, *AJ*, 96, 1649

Cudworth K. M., 1986, *AJ*, 92, 348

D'Antona F., Vesperini E., D'Ercole A., Ventura P., Milone A. P., Marino A. F., Tailo M., 2016, *MNRAS*, 458, 2122

D'Ercole A., Vesperini E., D'Antona F., McMillan S. L. W., Recchi S., 2008, *MNRAS*, 391, 825

D'Orazi V. et al., 2013, *ApJ*, 763, 22

Da Costa G. S., 2016, in Bragaglia A., Arnaboldi M., Rejkuba M., Romano D., eds, Proc. IAU Symp. Vol. 317, The General Assembly of Galaxy Halos: Structure, Origin and Evolution. Cambridge Univ. Press, Cambridge, p. 110

Da Costa G. S., Held E. V., Saviane I., Gullieuszik M., 2009, *ApJ*, 705, 1481

Dekker H., D'Odorico S., Kaufer A., Delabre B., Kotzlowski H., 2000, in Iye M., Moorwood A. F., eds, Proc. SPIE Conf. Ser. Vol. 4008, Optical and IR Telescope Instrumentation and Detectors. SPIE, Bellingham, p. 534

Di Matteo P., Spite M., Haywood M., Bonifacio P., Gómez A., Spite F., Caffau E., 2020, *A&A*, 636, A115

Marino A. F., 2015, preprint ([arXiv:1511.00330](https://arxiv.org/abs/1511.00330))

Fernández-Alvar E. et al., 2021, *MNRAS*, 508, 1509

Fernández-Trincado J. G. et al., 2017, *ApJ*, 846, L2

Fernández-Trincado J. G., Chaves-Velasquez L., Pérez-Villegas A., Vieira K., Moreno E., Ortigoza-Urdaneta M., Vega-Neme L., 2020, *MNRAS*, 495, 4113

Frebel A., Casey A. R., Jacobson H. R., Yu Q., 2013, *ApJ*, 769, 57

Freeman K. C., 1993, in Smith G. H., Brodie J. P., eds, ASP Conf. Ser. Vol. 48, The Globular Cluster-Galaxy Connection. Astron. Soc. Pac., San Francisco, p. 608

Freeman K. C., Rodgers A. W., 1975, *ApJ*, 201, L71

Frogl J. A., Persson S. E., Cohen J. G., 1983, *ApJS*, 53, 713

Gaia Collaboration, 2022, preprint ([arXiv:2208.00211](https://arxiv.org/abs/2208.00211))

- Gaia Collaboration, 2018, *A&A*, 616, A12
 Gaia Collaboration, 2021, *A&A*, 649, A1
 Gavagnin E., Mapelli M., Lake G., 2016, *MNRAS*, 461, 1276
 Goodfellow I., Bengio Y., Courville A., 2016, Deep learning. MIT press, Cambridge, MA
 Gratton R. G., 1982, *A&A*, 115, 171
 Gratton R. G., Ortolani S., 1989, *A&A*, 211, 41
 Gratton R. G., Carretta E., Bragaglia A., 2012, *A&AR*, 20, 50
 Gratton R. G. et al., 2014, *A&A*, 563, A13
 Gratton R., Bragaglia A., Carretta E., D'Orazi V., Lucatello S., Sollima A., 2019, *A&AR*, 27, 8
 Harding G. A., 1962, The Observatory, 82, 205
 Harris W. E., 1996, *AJ*, 112, 1487
 Heiter U., Jofré P., Gustafsson B., Korn A. J., Soubiran C., Thévenin F., 2015, *A&A*, 582, A49
 Hesser J. E., Harris G. L. H., 1979, *ApJ*, 234, 513
 Hesser J. E., Hartwick F. D. A., McClure R. D., 1976, *ApJ*, 207, L113
 Hesser J. E., Hartwick F. D. A., McClure R. D., 1977, *ApJS*, 33, 471
 Horta D. et al., 2020, *MNRAS*, 493, 3363
 Horta D. et al., 2021a, *MNRAS*, 500, 1385
 Horta D. et al., 2021b, *MNRAS*, 500, 5462
 Irrgang A., Wilcox B., Tucker E., Schiefelbein L., 2013, *A&A*, 549, A137
 Ji A. P. et al., 2020, *AJ*, 160, 181
 Jofré P. et al., 2015, *A&A*, 582, A81
 Johnson C. I., Pilachowski C. A., 2010, *ApJ*, 722, 1373
 Joo S.-J., Lee Y.-W., 2013, *ApJ*, 762, 36
 Joyce M., Chaboyer B., 2018, *ApJ*, 856, 10
 Kamann S. et al., 2018, *MNRAS*, 473, 5591
 Karakas A. I., Lattanzio J. C., 2014, *Publ. Astron. Soc. Aust.*, 31, e030
 Katz D., Gómez A., Haywood M., Snaith O., Di Matteo P., 2021, *A&A*, 655, A111
 Khoperskov S., Mastrobuono-Battisti A., Di Matteo P., Haywood M., 2018, *A&A*, 620, A154
 King I., 1961, *AJ*, 66, 68
 Kobayashi C., Karakas A. I., Lugaro M., 2020, *ApJ*, 900, 179
 Kordopatis G. et al., 2013, *MNRAS*, 436, 3231
 Kraft R. P., 1994, *PASP*, 106, 553
 Kraft R. P., Ivans I. I., 2003, *PASP*, 115, 143
 Lacchin E., Calura F., Vesperini E., 2021, *MNRAS*, 506, 5951
 Laird J. B., Wilhelm R. J., Peterson R. C., 1991, in Janes K., ed., ASP Conf. Ser. Vol. 13, The Formation and Evolution of Star Clusters. Astron. Soc. Pac., San Francisco, p. 578
 Lardo C. et al., 2015, *A&A*, 573, A115
 Lee J.-W., 2016, *ApJS*, 226, 16
 Lee J.-W., 2020, *ApJ*, 888, L6
 Lee J.-W., Carney B. W., Habgood M. J., 2005, *AJ*, 129, 251
 Lee J.-W., Kang Y.-W., Lee J., Lee Y.-W., 2009, *Nature*, 462, 480
 Legnardi M. V. et al., 2022, *MNRAS*, 513, 735
 Lehnert M. D., Bell R. A., Cohen J. G., 1991, *ApJ*, 367, 514
 Li C., Zhao G., 2017, *ApJ*, 850, 25
 Lim D., Han S.-I., Lee Y.-W., Roh D.-G., Sohn Y.-J., Chun S.-H., Lee J.-W., Johnson C. I., 2015, *ApJS*, 216, 19
 Lind K., Bergemann M., Asplund M., 2012, *MNRAS*, 427, 50
 Lindsay E. M., 1956, *Vistas Astron.*, 2, 1057
 Liu F., Yong D., Asplund M., Ramírez I., Meléndez J., 2016, *MNRAS*, 457, 3934
 Lloyd Evans T., 1977, *MNRAS*, 181, 591
 Lloyd Evans T., 1978a, *MNRAS*, 182, 293
 Lloyd Evans T., 1978b, *MNRAS*, 182, 293
 Mallia E. A., 1976a, *A&A*, 48, 49
 Mallia E. A., 1976b, *MNRAS*, 177, 73
 Manduca A., Bell R. A., 1978, *ApJ*, 225, 908
 Marino A. F., Milone A. P., Piotto G., Villanova S., Bedin L. R., Bellini A., Renzini A., 2009, *A&A*, 505, 1099
 Marino A. F. et al., 2011, *A&A*, 532, A8
 Marino A. F., Milone A. P., Lind K., 2013, *ApJ*, 768, 27
 Marino A. F. et al., 2015, *MNRAS*, 450, 815
 Marino A. F. et al., 2019, *ApJ*, 887, 91
 Martell S. L., Smolinski J. P., Beers T. C., Grebel E. K., 2011, *A&A*, 534, A136
 Martell S. L. et al., 2016, *ApJ*, 825, 146
 Massari D., Koppelman H. H., Helmi A., 2019, *A&A*, 630, L4
 Mastrobuono-Battisti A., Khoperskov S., Di Matteo P., Haywood M., 2019, *A&A*, 622, A86
 McKenzie M., Bekki K., 2018, *MNRAS*, 479, 3126
 McKenzie M., Bekki K., 2021, *MNRAS*, 507, 834
 Meléndez J., Asplund M., Gustafsson B., Yong D., 2009, *ApJ*, 704, L66
 Meléndez J. et al., 2012, *A&A*, 543, A29
 Mészáros S. et al., 2020, *MNRAS*, 492, 1641
 Milone A. P. et al., 2017, *MNRAS*, 464, 3636
 Monaco L., Pancino E., Ferraro F. R., Bellazzini M., 2004, *MNRAS*, 349, 1278
 Moreno E., Fernández-Trincado J. G., Pérez-Villegas A., Chaves-Velasquez L., Schuster W. J., 2022, *MNRAS*, 510, 5945
 Mucciarelli A., Bonifacio P., 2020, *A&A*, 640, A87
 Mucciarelli A., Lapenna E., Massari D., Pancino E., Stetson P. B., Ferraro F. R., Lanzoni B., Lardo C., 2015, *ApJ*, 809, 128
 Myeong G. C., Vasiliev E., Iorio G., Evans N. W., Belokurov V., 2019, *MNRAS*, 488, 1235
 Myeong G. C., Belokurov V., Aguado D. S., Evans N. W., Caldwell N., Bradley J., 2022, preprint ([arXiv:2206.07744](https://arxiv.org/abs/2206.07744))
 Nardiello D. et al., 2018, *MNRAS*, 477, 2004
 Neumayer N., Seth A., Böker T., 2020, *A&AR*, 28, 4
 Nissen P. E., Gustafsson B., 2018, *A&AR*, 26, 6
 Norris J., Bessell M. S., 1975, *ApJ*, 201, L75
 Norris J. E., Da Costa G. S., 1995, *ApJ*, 447, 680
 Norris J., Freeman K. C., 1983, *ApJ*, 266, 130
 Norris J. E., Ryan S. G., Beers T. C., 2001, *ApJ*, 561, 1034
 Peterson R. C., 1980, in Hesser J. E., ed., IAU Symposium Vol. 85, Star Clusters. Kluwer, Dordrecht, p. 461
 Peterson R. C., Cudworth K. M., 1994, *ApJ*, 420, 612
 Pfeffer J., Lardo C., Bastian N., Saracino S., Kamann S., 2021, *MNRAS*, 500, 2514
 Pilachowski C., Leep E. M., Wallerstein G., Peterson R. C., 1982, *ApJ*, 263, 187
 Piotto G. et al., 2012, *ApJ*, 760, 39
 Placco V. M., Sneden C., Roederer I. U., Lawler J. E., Den Hartog E. A., Hejazi N., Maas Z., Bernath P., 2021, *Res. Notes Am. Astron. Soc.*, 5, 92
 Ramírez I., Meléndez J., 2005, *ApJ*, 626, 465
 Ramírez I. et al., 2014, *A&A*, 572, A48
 Reggiani H., Meléndez J., Kobayashi C., Karakas A., Placco V., 2017, *A&A*, 608, A46
 Renzini A. et al., 2015, *MNRAS*, 454, 4197
 Richter P., Hilker M., Richtler T., 1999, *A&A*, 350, 476
 Roederer I. U. et al., 2008, *ApJ*, 679, 1549
 Roederer I. U., Sneden C., Thompson I. B., Preston G. W., Shectman S. A., 2010, *ApJ*, 711, 573
 Roederer I. U., Marino A. F., Sneden C., 2011, *ApJ*, 742, 37
 Santistevan I. B., Wetzel A., Sanderson R. E., El-Badry K., Samuel J., Faucher-Giguère C.-A., 2021, *MNRAS*, 505, 921
 Sawyer H. B., 1944, *Publ. David Dunlap Obs.*, 1, 294.2
 Schiavon R. P. et al., 2017, *MNRAS*, 465, 501
 Sestito F. et al., 2019, *MNRAS*, 484, 2166
 Shapley H., 1930a, *Star Clusters*. Vol. 2. Published for the Observatory by the McGraw-Hill Book Co, New York
 Shapley H., 1930b, *Harv. Coll. Obs. Bull.*, 874, 4
 Shapley H., Duncan J. C., 1922, *Publications of the American Astronomical Society*, 4, 48
 Shingles L. J., Karakas A. I., Hirschi R., Fishlock C. K., Yong D., Da Costa G. S., Marino A. F., 2014, *ApJ*, 795, 34
 Smith V. V., Suntzeff N. B., Cunha K., Gallino R., Busso M., Lambert D. L., Straniero O., 2000, *AJ*, 119, 1239

- Sneden C., 1973, *ApJ*, 184, 839
 Sneden C., Kraft R. P., Shetrone M. D., Smith G. H., Langer G. E., Prosser C. F., 1997, *AJ*, 114, 1964
 Sneden C., Johnson J., Kraft R. P., Smith G. H., Cowan J. J., Bolte M. S., 2000, *ApJ*, 536, L85
 Sollima A., Baumgardt H., Hilker M., 2019, *MNRAS*, 485, 1460
 Stetson P. B., Pancino E., 2008, *PASP*, 120, 1332
 Straniero O., Cristallo S., Piersanti L., 2014, *ApJ*, 785, 77
 Tautvaišienė G., Viscasillas Vázquez C., Mikolaitis Š., Stonkutė E., Minkevičiūtė R., Drazdauskas A., Bagdonas V., 2021, *A&A*, 649, A126
 Tautvaisiene G. et al., 2022, *A&A*, 658, A80
 Thévenin F., Idiart T. P., 1999, *ApJ*, 521, 753
 van den Bergh S., 1996, *ApJ*, 471, L31
 Vasiliev E., 2019, *MNRAS*, 489, 623
 Vasiliev E., Baumgardt H., 2021, *MNRAS*, 505, 5978
 Ventura P., Caloi V., D'Antona F., Ferguson J., Milone A., Piotto G. P., 2009, *MNRAS*, 399, 934
 Wallerstein G., Leep E. M., Oke J. B., 1987, *AJ*, 93, 1137
 Woolley R. V. D. R., 1966, *R. Obs. Ann.*, 2, 1
 Yong D., Grundahl F., 2008, *ApJ*, 672, L29
 Yong D., Grundahl F., D'Antona F., Karakas A. I., Lattanzio J. C., Norris J. E., 2009, *ApJ*, 695, L62
 Yong D. et al., 2013, *MNRAS*, 434, 3542
 Yong D. et al., 2014a, *MNRAS*, 441, 3396
 Yong D. et al., 2014b, *MNRAS*, 441, 3396

SUPPORTING INFORMATION

Supplementary data are available at [MNRAS](https://www.mnras.org/) online.

sup_linelist.csv

Please note: Oxford University Press is not responsible for the content or functionality of any supporting materials supplied by the authors. Any queries (other than missing material) should be directed to the corresponding author for the article.

APPENDIX A: RADIAL VELOCITIES

We provide the heliocentric radial velocities for our stars, along with a comparison to the literature in Table A1. This is only a subset of published measurements and not an exhaustive list of values in the literature. Our values are in good agreement to those from Gaia DR3 (Gaia Collaboration 2022).

APPENDIX B: DETAILS ON ROUTINE FOR EVALUATING AND INSPECTING EQUIVALENT WIDTHS (REVIEW)

We developed our own code to determine the EWs of lines in our program stars (available from <https://github.com/madeleine-mckenzie/REVIEW>). One advantage of this code over others currently in use is that it does not require additional package installs that are not regularly used in the PYTHON language. Synthetic spectra were generated to span a range of EWs, possible locations of a line, and deviations from a normalised continuum.

Normalized line depths spanned from 0.06 to 0.7, line widths from 0.03 to 0.15 Å, line positions between ± 0.2 Å from the predicted location in the line list, and continuum values ± 0.02 from the normalized continuum. These ranges were chosen to be consistent with the variation found in our target stars. Up to 4 Gaussian lines are placed within the 1.2 Å window in which we fit our lines to account for blended lines and various degrees of random noise are added to the spectra to allow for EW measurements for spectra at lower S/N regions.

We train a FFNN on the synthetic spectra to validate the EWs recovered through `curve_fit`. The FFNN is trained with the ReLU activation function, maximum 500 iterations, 10^{-4} tolerance, and 10 per cent holdout. We do a hyperparameter search over layers, neurons, and the L2 penalty and find the best hyperparameters to be 4 layers, 300 neurons, and L2 penalty of 10^{-5} . Our best hyperparameters are picked based upon a labelled real data set as opposed to the synthetic data set. We note that this does cause data leakage but as we are only testing the validity of our results with the FFNN and not using the actual values, this data leakage should not affect our final results.

Our real data are not always sampled in the same way as our synthetic spectra, and thus we interpolate over each line using a cubic spline. The choice of interpolation function has no statistical impact on the determination of the EW. Although interpolation of the data is necessary to account for different pixel sizes and FWHM.

It does slightly decrease the accuracy of the neural network (± 2 mÅ for our validation data). We provide an example of the output of one star in Fig. B1 and B2. More detailed explanations of each of the returned quantities is provided on the github page.

Table A1. Heliocentric radial velocities as measured by our study along with a sample of literature values.

	This work	Peterson & Cudworth (1994)	Cote et al. (1996)	Marino et al. (2011)	Alves-Brito et al. (2012)	Gaia Collaboration (2022)
C	−149.05	-	−154.32	-	-	−151.40
III-3	−146.48	−147.46	−148.26	−148.16	−148.6	−146.94
III-14	−150.80	−152.72	−150.98	-	−150.2	−149.78
III-15	−146.46	−144.45	−147.47	-	−148.3	−145.58
III-52	−150.66	−150.40	−151.95	−153.22	−148.8	−149.95
IV-102	−137.87	−142.29	−140.71	-	−149.1	−140.14

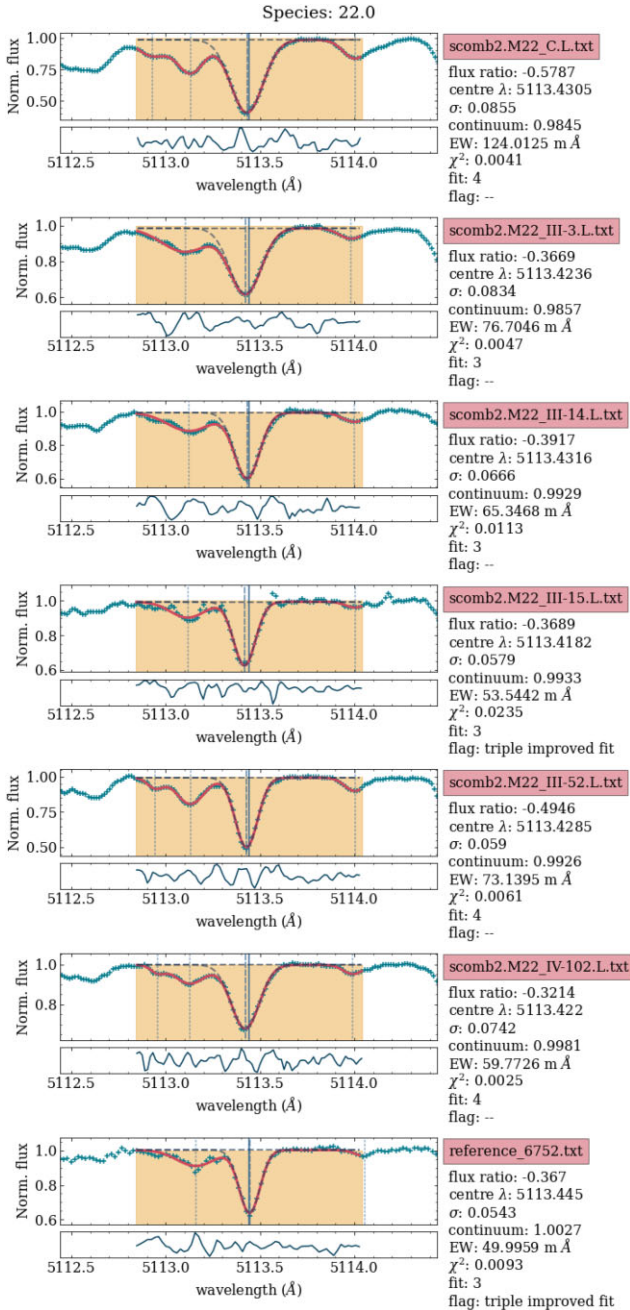


Figure B1. An example output from our EW fitting code REVIEW. An image is generated for each line in the line list so that the quality of fitting can be determined by eye. We plot a titanium line with additional absorption features to the blue and red. For each panel, the spectra (green crosses) has been fit by a variable number of Gaussians within the yellow region, and we can confirm that both the line and the continuum has been fitted correctly. In higher S/N spectra, the algorithm identifies four lines in this region without the need for a detailed line list. Where there is more noise, it reverts to three Gaussians to model the line.

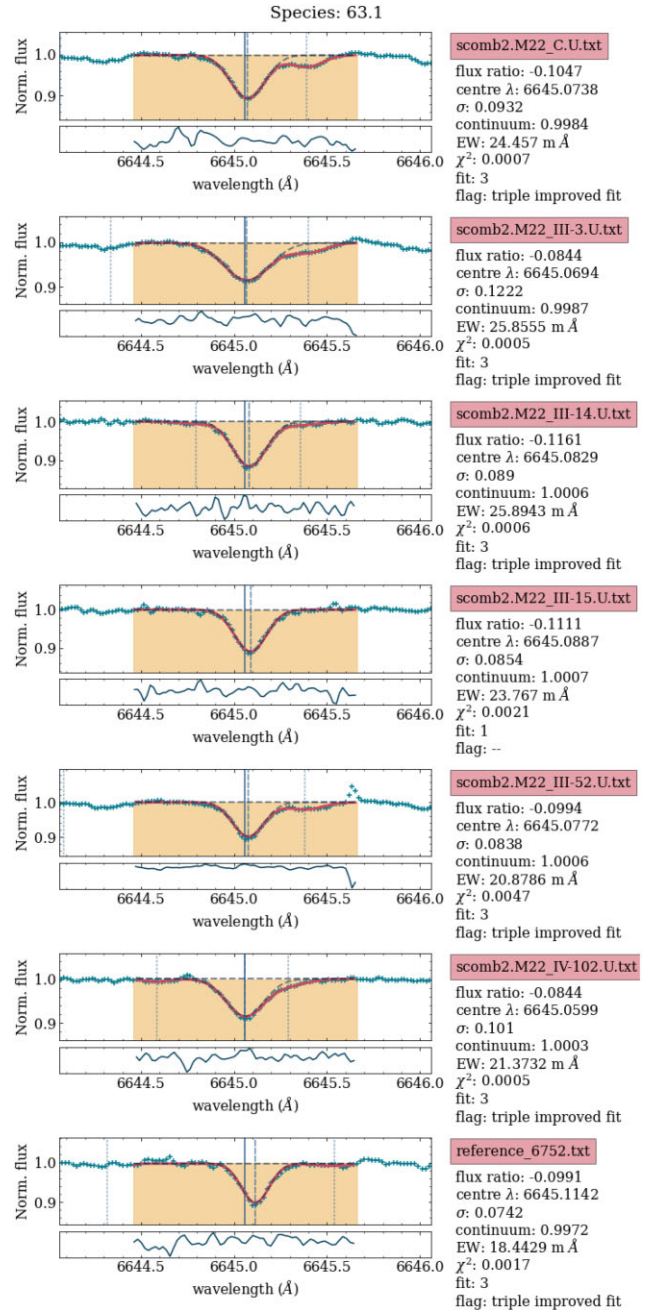


Figure B2. The same as Fig. B1 but for the r -process element Eu. The code can still correctly measure the line, despite the blended iron line to the right.

APPENDIX C: STELLAR PARAMETERS FROM THE LITERATURE

See Table C1 for a compilation of literature values for the stellar parameters of our sample stars. We list the Fe I values for Mucciarelli et al. (2015).

Table C1. Literature values of stellar parameters for our program stars.

Publication	C	III-3	III-14	III-15	III-52	IV-102
	T_{eff} (K)					
Peterson (1980)	–	4000	–	–	–	–
Gratton (1982)	–	–	–	–	4150	–
Pilachowski et al. (1982)	–	4100	–	–	–	3900
Frogel et al. (1983)	–	4165	4062	–	4192	4086
Wallerstein et al. (1987)	–	4150	–	–	–	4050
Gratton & Ortolani (1989)	–	–	–	–	4192	–
Brown et al. (1990)	–	4500	–	–	4200	4400
Brown & Wallerstein (1992)	–	4165	–	–	4200	4090
Marino et al. (2009)	–	3990	–	–	4100	–
Marino et al. (2011)	3960	4000	4030	4070	4075	4020
Alves-Brito et al. (2012)	–	3952	3919	4055	4124	3974
Mucciarelli et al. (2015) (method 1)	–	3910	–	–	4060	–
Mucciarelli et al. (2015) (method 2)	–	3960	–	–	4070	–
Mucciarelli et al. (2015) (method 3)	–	3992	–	–	3986	–
This work	3912	4041	4038	4136	4100	4043
Average	3936	4071	4012	4087	4121	4070
	$\log g$ (cm s ⁻²)					
Gratton (1982)	–	–	–	–	0.3	–
Pilachowski et al. (1982)	–	0.7	–	–	–	0.9
Frogel et al. (1983)	–	0.5	0.5	–	0.8	0.5
Wallerstein et al. (1987)	–	0.5	–	–	–	0.5
Gratton & Ortolani (1989)	–	–	–	–	0.8	–
Brown et al. (1990)	–	0.7	–	–	0.8	0.5
Brown & Wallerstein (1992)	–	0.5	–	–	0.8	0.5
Marino et al. (2009)	–	0.2	–	–	0.67	–
Marino et al. (2011)	0.3	0.3	0.35	0.4	0.6	0.2
Alves-Brito et al. (2012)	–	0.43	0.41	0.59	0.72	0.43
Mucciarelli et al. (2015; method 1)	–	0.4	–	–	0.57	–
Mucciarelli et al. (2015; method 2)	–	0.34	–	–	0.63	–
Mucciarelli et al. (2015; method 3)	–	0.36	–	–	0.65	–
This work	0.105	0.25	0.12	0.45	0.51	0.1
Average	0.20	0.43	0.35	0.48	0.65	0.45
	[Fe/H]					
Peterson (1980)	–	–1.62	–	–	–	–
Gratton (1982)	–	–	–	–	–1.89	–
Pilachowski et al. (1982)	–	–1.35	–	–	–	–1.7
Wallerstein et al. (1987)	–	–1.5	–	–	–	–1.7
Gratton & Ortolani (1989)	–	–	–	–	–1.7	–
Brown et al. (1990)	–	–1.7	–	–	–1.6	–1.9
Brown & Wallerstein (1992)	–	–1.55	–	–	–1.56	–1.78
Marino et al. (2009)	–	–1.66	–	–	–1.62	–
Marino et al. (2011)	–1.60	–1.72	–1.82	–1.82	–1.63	–1.97
Alves-Brito et al. (2012)	–	–1.62	–1.64	–1.72	–1.54	–1.87
Mucciarelli et al. (2015; method 1)	–	–1.84	–	–	–1.72	–
Mucciarelli et al. (2015; method 2)	–	–1.8	–	–	–1.7	–
Mucciarelli et al. (2015; method 3)	–	–1.8	–	–	–1.68	–
This work	–1.70	–1.78	–1.87	–1.83	–1.71	–1.97
Average	–1.65	–1.66	–1.78	–1.79	–1.67	–1.84

This paper has been typeset from a \LaTeX file prepared by the author.